NOTE TO USERS

This reproduction is the best copy available.

UMI®

Stability Investigation at Resonance of Surface Micromachined Comb Drive for Application as a Power Source

Yanxia Zhang

A Thesis

In

The Department

of

Electrical and Computer Engineering

Presented in Partial Fulfillment of the Requirements
for the Degree of Master of Applied Science at
Concordia University
Montreal, Quebec, Canada

March 2005

© Yanxia Zhang, 2005

Library and Archives Canada

Published Heritage Branch

395 Wellington Street
Ottawa ON K1A 0N4
Canada

Bibliothèque et Archives Canada

Direction du Patrimoine de l'édition

395, rue Wellington
Ottawa ON K1A 0N4
Canada

Your file Votre référence
ISBN: 0-494-04409-8
Our file Notre référence
ISBN: 0-494-04409-8

NOTICE:
The author has granted a non-exclusive license allowing Library and Archives Canada to reproduce, publish, archive, preserve, conserve, communicate to the public by telecommunication or on the Internet, loan, distribute and sell theses worldwide, for commercial or non-commercial purposes, in microform, paper, electronic and/or any other formats.

The author retains copyright ownership and moral rights in this thesis. Neither the thesis nor substantial extracts from it may be printed or otherwise reproduced without the author's permission.

AVIS:
L'auteur a accordé une licence non exclusive permettant à la Bibliothèque et Archives Canada de reproduire, publier, archiver, sauvegarder, conserver, transmettre au public par télécommunication ou par l'Internet, prêter, distribuer et vendre des thèses partout dans le monde, à des fins commerciales ou autres, sur support microforme, papier, électronique et/ou autres formats.

L'auteur conserve la propriété du droit d'auteur et des droits moraux qui protège cette thèse. Ni la thèse ni des extraits substantiels de celle-ci ne doivent être imprimés ou autrement reproduits sans son autorisation.

In compliance with the Canadian Privacy Act some supporting forms may have been removed from this thesis.

While these forms may be included in the document page count, their removal does not represent any loss of content from the thesis.

Conformément à la loi canadienne sur la protection de la vie privée, quelques formulaires secondaires ont été enlevés de cette thèse.

Bien que ces formulaires aient inclus dans la pagination, il n'y aura aucun contenu manquant.

ABSTRACT

Stability Investigation at Resonance of Surface Micromachined Comb Drive for Application as a Power Source

Yanxia Zhang

The comb drive has direct application in micromachined mechanisms such as optical switches, electrical switches or any other microsized devices requiring mechanical power. In most cases a cantilever beam is attached to one side of the moving plate, perpendicular to the length of folded springs, either to transfer motion or for optical switching. However, the asymmetry of the comb drive may lead to system instability or failure due to rotational motion. The stability at high frequency is especially important because it is essential for reliable high-speed optical switching.

This thesis presents the results of an on-going research on fundamental issues related to comb drive and the feasibility of the microengine driven by the comb drives. Mechanical analysis and electrical properties are addressed and modeled. In order to suppress rotational motion due to the asymmetry, "balanced comb drive" with torque balance is proposed. Attention is mostly focused on the stability at high frequency in the cases where a cantilever is attached to the comb drive, either for transferring motion to coupling structure or for optical switching. Different measurement approaches in frequency domain are discussed. Theoretical formulas are derived and analyzed.

In this work, both balanced and unbalanced comb drives, with or without rack and pinion engagement are fabricated using MUMPs technology. Post-processing, including HF release, application of lubricant and bonding is carried out afterwards. Experiments in probe station and SEM, and frequency domain measurements at

atmosphere are carried out. Balanced comb drives exhibit superior stability both in SEM observation and spectrum analysis.

ACKNOWLEDGEMENT:

I would like to take this opportunity to thank the many individuals who have contributed to my personal and academic growth over the past two years in Concordia University.

First of all, I would like to thank my research supervisor, Dr. Mojtaba Kahrizi, who introduced me to MEMS and sparked my interest in it. He has guided me through my two-year's research and drove me to excel. He is influential in making this work a success. I learned a great deal about large displacement actuators from him. He gave me the opportunity to work in this field both technically and financially.

I would like to thank the past and present members of the Semiconductor team in Concordia University, for their technical discussion and help. I would like to thank Mr. Shailesh Prasad, for his kindly assist in clean room work and Mr. Jun Chen for his kind help with SEM measurement and Mr. Oleg Grudin for his tutorial on the bonding machine.

Finally, I would like to thank my parents Buhuai Zhang and Xianfeng Liu for their never-ending love, support and guidance throughout the path leading me to Concordia University. Without them, I would not be here today.

TABLE OF CONTENTS

LIST OF FIGURES......viii

LIST OF TABLES......xii

CHAPTER 1 INTRODUCTION 1

1.1 Literature Review......4

1.1.1 Large Displacement Actuators......4

1.1.2 Microtribology and Micromechanics of MEMS Devices......6

1.1.3 Frequency Domain Measurement......9

1.2 Thesis Outline......11

1.3 Summary of the Work in This Thesis......13

CHAPTER2: DESIGN PRINCIPLE 14

2.1 Design Principle......14

2.1.1 Comb Drive Design......15

2.1.2 Rack and Pinion Design......16

2.2 Comb Drive Mechanical Analysis......20

2.2.1 Resonant Frequency......20

2.2.2 Slide Film Damping......24

2.2.3 Quality Factor Q......26

2.2.4 Comb Drive System Model......28

2.3: Comb Drive Electrical Analysis......33

2.3.1 Lateral Displacement and Vertical Levitation Mechanism......33

2.3.2 Fringing Effect......38

2.3.3 Equivalent Circuit......38

CHAPTER 3: FABRICATION AND POST-PROCESSING 41

3.1 Design Implementation..41

3.2 Post-Processing..42

3.2.1 HF Release..42

3.2.2 Application of Lubricants..44

CHAPTER 4: MEASUREMENT THEORY 51

4.1 Frequency Doubling Measurement..53

4.2 Mixing Frequency Measurement..57

CHAPTER 5: EXPERIMENTAL RESULT 67

5.1 Experimental Instruments..67

5.1.1 Micro Manipulation Probe Station..67

5.1.2 Hitachi S-520 Scanning Electron Microscope..68

5.1.3 SR770 FFT Spectrum Analyzer (DC-100kHz)..69

5.1.4 Tektronix 2710 Spectrum Analyzer (1MHz – 1.2 GHz)..71

5.2 Time Domain Experimental Data..72

5.2.1 Probe Station Observations..72

5.2.2 SEM Observations..75

5.3 Frequency Domain Data..83

CHAPTER 6: CONCLUSION AND FUTURE WORK 87

REFERENCE 88

PUBLICATION 91

LIST OF FIGURES

1.1 Schematic drawing of surface micromachined microengine, where comb drive used as power source. The expanded view in the lower right corner is the link-gear arrangement[3]..2

1.2 Optical switch driven by electrostatic comb drive[5]................................3

1.3 SEM video images of operating DMD. The left mirrors are -10°, while the right mirrors are +10° [9]..5

1.4 The schematic of a lateral resonant comb drive..6

2.1 CADENCE layout of large lateral displacement actuator..........................14

2.2 a) the original gear system without displacement b) the rack moves 5 μm to the right, the pinion rotates 7 degrees, as shown in the outline. c) The rack moves another 5 μm; the pinion will rotate another 12 degrees. In both situations, the rack and pinion will not block. In this design, the inner radius is 10 μm and the outer radius is 20 μm. Thus according the figure, the pinion rotates 19 degree totally for 10 μm displacement..15

2.3 The contact point of involute gear..17

2.4 a) the layout of rack and pinion, with slide proof support underneath and stop anchor on the right; b) the cross-section of the gear..................................19

2.5 The modeling of the rack and pinion motion..20

2.6 Mode shape of a folded beam support when the resonant plate is displaced by X_0 under a force of F_x [6]..21

2.7 The first three resonant modes of standard comb drive： a) lateral resonance; b) vertical resonance; c) rotational resonance..22

2.8 The displacement contour plots of the first three resonant modes of the balanced design: a) the lateral resonant mode; b) the vertical resonant mode and c) the rotational resonant mode......23

2.9 Displacement contour plot in Z direction at lateral resonant mode......24

2.10 Q can be determined through the resonant frequency and the –3dB bandwidth..27

2.11 Viscous underdamped oscillation......29

2.12 System model built with Ansys......30

2.13 System reaction under electrical impulse stimulation; the impulse is 50v and lasts for $3*10^{-6}$s......32

2.14 Matlab verification, a) full time range, b) zoom in......32

2.15 Discrete energy spectrum of comb drive......33

2.16 Electrostatic analysis model......34

2.17 The potential distribution 37

2.18 The electrical field vector plot simulated using COSMOSEMS: a) front view; b) cross-section view......37

2.19 The variation of fringing constant versus structure thickness......38

2.20 Circuit elements' electrical properties......39

2.21 The equivalent circuit for the comb drive......40

3.1 Cross-sectional view of a micromotor using POLYMUMPs, a) before releasing; b) after releasing......41

3.2 Stimulation of the device with a micromanipulator......43

3.3 Microscope observations of the device. a) Large lateral displacement actuator; b) rotation due to fluidic force, small rotation angle leads to large displacement at the tip of the beam; c) different gear tooth design......44

3.4 Observation of large friction between POLY1 and POLY0, when no supporting dimples at the ends of springs...46

3.5 West Bond 7476E Wire Bonding machine..49

4.1 The current frequency components...53

4.2 The amplitude ($Amp(\omega_d)$) of motional current in logarithm axis..................56

4.3 a) Schematic of mixing frequency measurement for spectrum analysis; b) equivalent circuit of the resonator shown in a); c) current spectrum at the sensing electrode; d) the spectrum after demodulation...58

4.4 Plot of frequency response at atmosphere..64

4.5 Comparison of spectrum with different spring constants at atmosphere............65

4.6 Comparison of spectrum operating at different levels of pressures..................65

5.1 HITACHI S-520 Scanning Electron Microscope and its block diagram 69

5.2 a) sampled time domain waveform and the resulting frequency domain plot using Fast Fourier Transform...70

5.3 SR770 FFT Spectrum Analyzer...71

5.4 Tektronix 2710 Spectrum Analyzer..72

5.5 a) the connection diagram of LM741; b) the circuit configuration of inverter.....73

5.6 Circuit schematic indicating the electrical connections necessary for driving a lateral resonant microstructure into resonance in probe station..........................74

5.7 The probe observation of the vibration, a) the spring blur, b) the layout of the scale, b) the blur of the cantilever beam tip...75

5.8 Unbalanced (a) comb drive for testing and balanced (b) comb drive as power source...76

5.9 SEM observation of sink of movable fingers when no voltage is applied..........77

5.10 Circuit schematic indicating the electrical connections necessary for driving a lateral resonant microstructure into resonance in SEM....................................79

5.11 Predicted resonant frequency (blue) and the measured resonant frequency (red) for balanced comb drive...80

5.12 SEM observation of comb drive under test. a) wave propagation along the fingers at resonant frequency; b) wave propagation along the folded beam at resonant frequency and c) wave propagation along the fingers at half resonant frequency...82

5.13 The resonant mode of balanced comb drive..83

5.14 Circuit schematic used for mixing frequency measurement........................84

5.15 Output spectrum for balanced comb drive measured at air pressure...............85

5.16 Plot of quality factor at atmosphere versus folded-beam length....................85

5.17 Output spectrum for unbalanced comb drive, measured at air pressure. (Y-axis:5dB/div and X-axis:5kHz/div) 86

LIST OF TABLE

2.1 Unbalanced Comb Drive Parameters and geometry parameters.........................23

2.2 Geometry, material properties and damping coefficient used for simulation......30

3.1 Layer names, thickness and lithography levels of POLYMUMPs [33].............42

3.2 Available Grades and Typical Physical Properties of Fomblin PFPE Lubricant Z DOL 2000..47

3.3 Available Grades and Typical Physical Properties of Fomblin PFPE Lubricant Z 03..47

3.4 Available Grades and Typical Physical Properties of Galden PFPE HT55 and HT70..48

3.5 Type of wire and parameter settings..49

4.1 The system parameters..55

4.2 The System Parameters..64

5.1 The main parameters of SR770 FFT Spectrum Analyzer............................71

5.2 Balanced and unbalanced Comb Drive Parameters..................................79

5.3 Measured quality factor in SEM..80

Chapter 1: Introduction

There exist a variety of instances where a microsized power source is required to actuate a micromechanism, supplying either linear or rotating motion. Previously demonstrated micromotors might be used if a means for low starting voltage, high rotating speed and less friction are achieved [1,2]. An alternative approach is electrostatic comb drive with folded springs, which is widely used because it offers large linear deflection range and high stiffness ratio between vertical and lateral motions.

The comb drive has direct application as a power source for micromachined mechanisms such as optical switches, electrical switches, micro-positioner or any other microsized devices require mechanical power [3]. In most cases where comb drive used as power source, a cantilever beam is attached to the moving plate, perpendicular to the length of folded springs, such as the surface micromachined microengine [3] made by Sandia National Laboratories as shown in figure 1.1, integrated gear linkages [4] and the vertical micromirror arrays for optical switching [5], as shown in figure 1.2. Optical MEMS, especially in optical fiber communication, is considered to be the mainstream technology to fulfill the missing link that connecting other existing technologies to form the all-optical network. Optical switches with the similar mechanism as shown in figure 1.2 developed at University of Neuchatel, are fabricated and successfully commercialized by a start-up company named Sercalo Microtechnology.

However, in these cases, the asymmetry of the comb drive may lead to system failure due to rotational motion. Even though several successful system operations are

demonstrated [3-5], and detailed theoretical analysis, simulations and experimental results of standard comb drive are reported [6-8], no research is carried out on the behaviour of comb drive with an attached cantilever beam.

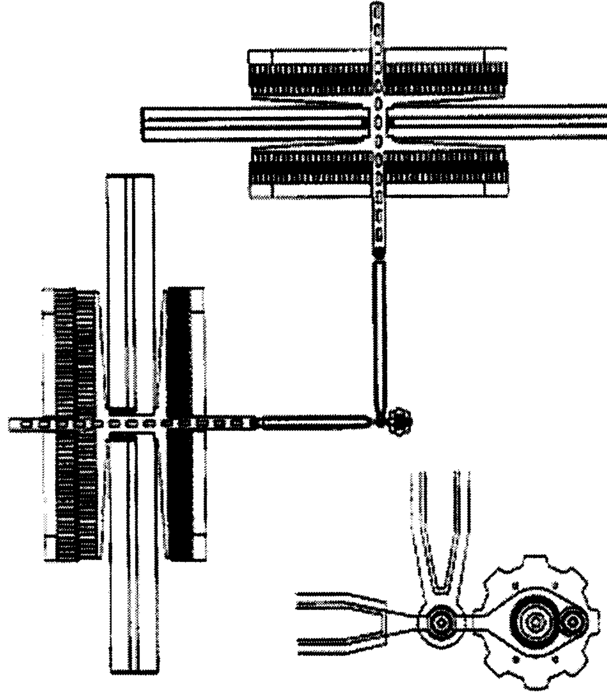

Figure 1.1: Schematic drawing of surface micromachined microengine, where comb drive used as power source. The expanded view in the lower right corner is the link-gear arrangement [3]

In this work, both mechanical and electrical properties of comb drive are addressed; special issues of comb drive with an attached beam are discussed. Unbalanced comb drives and balanced comb drives, with and without rack and pinion engagement, are fabricated and tested in probe station and SEM chamber. Theoretical formulas governing the spectrum are experimentally verified. In both SEM observations and spectrum analysis, balanced comb drives present superior stability over unbalanced comb drives.

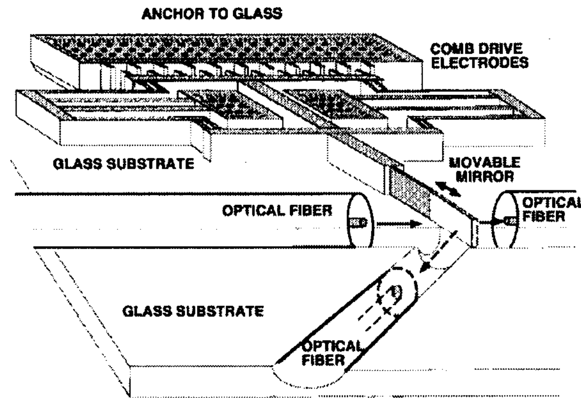

Fig. 1.2: Optical switch driven by electrostatic comb drive [5]

The Primary goal of this thesis is to design, fabricate and test comb drives with an attached cantilever beam and the feasibility of microengine driven by these comb drives. The challenge of this work is verify the concept "balanced comb drive used as power source" and push the limits of surface micromachining and electromechanical design, subject to the constraints: requirement for large displacement and overcoming of the stiction and air damping. Specifically, the displacement is limited by the small electrostatic force generated by the $2\,\mu m$-thick polysilicon; overcoming of the static friction forces (stiction) and air damping is critical because of the continuous contact between gear and hub bearing, teeth, and contacts between dimples and POLY0/silicon nitride.

The design and measurement must consider significant challenges and parameters including device features, residual stress, stiction, air damping, lubrication and large horizontal displacement.

1.1 Literature Review

1.1.1 Large Displacement Actuators

Micro electromechanical systems (MEMS) refer to the fabrication of devices with some part of their dimensions in the micrometer range. MEMS are used in various fields, including aerospace, optical communication system, wireless communication, robotics, chemical systems, biotechnology and microscopy. Microfabrication technology for MEMS includes surface micromachining, bulk micromachining and LIGA. The MEMS devices are batch fabricated, similar to devices produced in semiconductor industry. MEMS are used either as sensors, which convert mechanical energy to some other energy, or as actuators, which can transfer energy in some domain into mechanical response. The design presented in this thesis is an actuator.

With regard to actuators, we can divide the subject into electrostatic actuators, magnetic actuators, fluidic actuators, thermal actuators, chemical actuators and electrochemical phenomena, according to the domain that energy transfers from. Electrostatic actuators exert an attractive force on oppositely charged objects or a repulsive force on similarly charged ones. Examples of this kind of actuators are DMD device by Van Kesel [9], an electrostatic microvalve by Sato et.al. [10]; wobble micromotor by T.Guruhata, et al [11]. Magnetic actuators result from the force generated in a magnetic field; the field is generated by passing a current through a surface coil. Examples include high-performance magnetographic printing heads [12], electronic switching components [13] and different types of vertical, torsional and multi-axial

actuators. Fluid mechanics deals with the motion of fluids and the forces associated with the motion. Fluid and surface interactions, such as capillary forces, become more significant with smaller fluidic channels, for example, passive valve by changing the diameter of capillary conduits and capillary burst valves on a centrifugal fluidic platform [14]. Thermal actuators cause bending or deformation by temperature difference or different thermal expansion coefficients (Thermally Actuated Valves [15]). Chemical actuators utilize special chemical properties that can change the response in the other domain, such as the polymer solutions and surfactant solutions, which are used to reduce the turbulent drag [16].

For optical applications there are four types of actuators: vertical, lateral, flip-up and torsion. Flip-up mirrors are used for optical benches [11] and torsion mirror are used to process light in reflective applications or in displays, like DMD. Vertical displacement allows diffractive applications such as GLV but usually confined to small displacement. Lateral displacement actuators can typically be converted to large-scale motion. The work presented in this thesis is lateral displacement actuators.

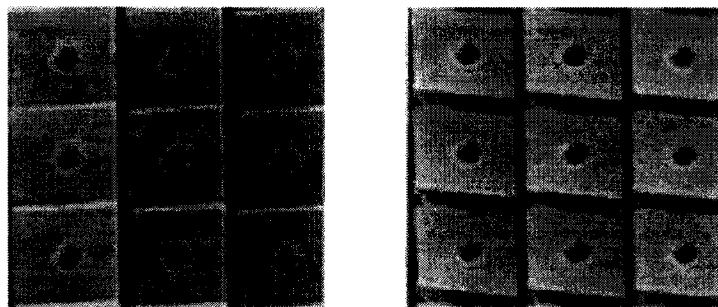

Figure 1.3: SEM video images of operating DMD. The left mirrors are -10°, while the right mirrors are +10° [9]

Electrostatic comb drive first emerged in 1989. The key feature of the comb drive

is that $\partial C / \partial x$ is a constant, independent of the displacement x, as long as x is less than the finger overlap [8]. A schematic plot of standard comb drive is shown in figure 1.4. Because of the linearity of electromechanical transfer, large displacement ($10\,\mu m$ for $200\,\mu m$-long support springs) and high resonant frequency (72kHz for $80\,\mu m$-long support springs), the comb drive has been widely as driven force for MEMS device, such as two-dimensional manipulator [6]. Later more fabrication optimization has been made, including an effort to reduce the gap between fingers in order to increase electrostatic force [17], process model which determines the offset and sidewall angle of beams [18]. Failure modes and stability of comb drive has been addressed by S.L.Miller [19]. According to the advantages mentioned above, electrostatic comb drive will be used as power source in this work.

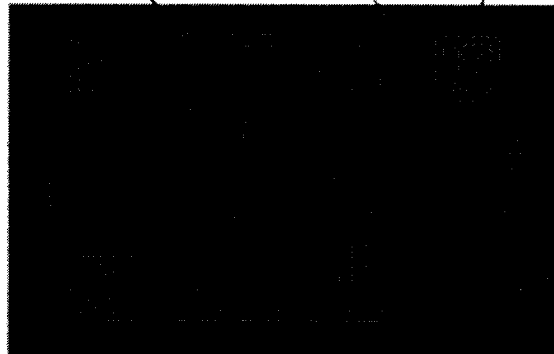

Figure 1.4: The schematic of a lateral resonant comb drive

1.1.2 Microtribology and Micromechanics of MEMS Devices

Tribology becomes a critical key when one considers the motions of very small bodies in which micrograms or even less are proper units of mass. The surface forces such as friction, adhesion, meniscus forces, viscous drag and surface tension that are

proportional to area become a thousand times larger than the forces proportional to the volume, such as inertial and electromagnetic force [20]. The nature of friction on this tiny scale is in need of fundamental study.

A major challenge for MEMS is to overcome the effect of stiction. The term stiction is used to describe two circumstances: (1) sticking of a "freed" member together with the newly exposed surface underneath the sacrificial layer after the final "freeing" etch step of the micromachining process, and (2) adherence of two mechanical microparts that approach or touch one another when the microsystem is in operation [21], or defined as static friction.

The final step, sacrificial etching, usually causes sticking due to surface tension during the drying stage. When the etching dissolves the sacrificial layer, adjacent surfaces result in menisci that lead to attractive forces. These forces can buckle the "freed" member and possibly cement it to the underlying surface [21]. Mechanical analysis of release-stiction effects has been performed (Mastrangelo, 1997); design optimization experiments have been carried out by H.Berney et al [22] and Meng-Ju Lin [23]; and post-processing, like rinse in water-methanol, can eliminate surface tension effectively [24]. Following these disciplines to design and release, large surface-micromachined structures may be processed successfully.

Static friction force (stiction) is the main retarding force in MEMS devices because of the high surface-to-volume ratio. A large lateral force is required to initiate relative motion between two smooth surfaces. In early works, device failure due to

stiction is the major problem for micromotors and gear systems, such as the gear system failure modes reported by Sandia National Laboratories [19] and micro-side-drive motors' static friction characteristics [25]. Various lubrication methods and measurement results are demonstrated later, such as micromotor's successful operation in deionized water and silicone lubricating oil [26]; various monomolecular layers with different process [27] and effect of bonded lubricant films on friction and durability [28]. Optimization in fabrication also have been made to improve surface roughness, for example, a polysilicon surface roughness near 0.8nm rms is produced by increasing temperature to $591^{\circ}C$ in LPCVD [24].

In V.R.Dhuler's work [26], the minimum operating voltages for micromotors in liquid are typically more than two times higher for operation in the air, while the maximum motor speeds possible are significantly lower. The motive torque is increased by the relative dielectric constant of the liquid, while the viscous drag torque is increased due to the high viscosity of the liquid. Because of the complicated nature of the liquid, the lower speed and higher operating voltage and viscous drag torque, we will not consider this lubricant in this thesis.

As mentioned above, H.Zarrad et al [27] discussed the stiction measurement on monomolecular layers fabricated by Langmuir-Blodgett process or Kovats' Process. The coefficient of friction is lowered from 0.6 for bare silica to a minimum of 0.07. However, the result is chemical sensitive and the monolayer is not dense enough to resist to the friction and achieve long durability.

For bonded lubricant, According to publications [29] [30] [31], the lubricant film thickness can be controlled by the solution concentration and withdrawal speed, while the bonded thickness is a function of soaking time, baking time and baking temperature and applied lubricant thickness. Measurement of micromotor's static friction force as a function of bonded lubricant thickness, rest time and relative humidity is conducted by S.Sundararajan and B.Bhushan [20]. Consider the equipments, process limitation and well-defined process and sufficient experiment data of bonded lubricant, nonpolar and polar perfluoropolyether bonded films will be used in this thesis.

1.1.3 Frequency domain measurements

The pioneer of spectrum analysis was undoubtedly Hermann von Helmholtz, using a series of hollow glass spheres with carefully calibrated resonance frequencies to analysis the sound spectrum. While nowadays Fourier transforms provides a useful mathematical relation between a waveform and the phase amplitude density of its frequency contents, i.e., it resolves a waveform into its sinusoidal component.

Most machine-train failures results at or near a frequency component associated with the running speed. Therefore, the ability to display and analyze the vibration spectrum as components of frequency is extremely important. The real advantage of the frequency-domain analysis is the ability to normalize each vibration component so that a complex machine-train spectrum can be divided into discrete components. This ability simplifies isolation and analysis of mechanical degradation within the machine-train. In addition, note that frequency-domain analysis can be used to determine the phase

relationships for harmonic vibration components in a typical machine-train spectrum. The frequency domain normalizes any or all running speeds, where as time-domain analysis is limited to true running speed.

The frequency-domain format eliminates the manual effort required to isolate the components that make up a time trace. Frequency-domain techniques covert time-domain data into discrete frequency components using a fast Fourier transform. Simply stated, FFT mathematically converts a time-based trace into a series of discrete frequency components. In a frequency-domain plot, the X-axis is frequency and the Y-axis is the amplitude of displacement, velocity, or acceleration.

In order to realize numerical evaluation of the transform, discrete Fourier transform (DFT) is used. This has two advantages. First, many of the ideas and methods of time series analysis can be borrowed and used for the present purposes. Second, it allows the use of the very efficient fast Fourier transform (FFT) computer algorithm [32]. The discrete Fourier transform of a sequence of N complex numbers $\{x_0, x_1, \ldots\ldots, x_{N-1}\}$ is another sequence of N complex numbers $\{X_0, X_1, \ldots\ldots, X_{N-1}\}$, where

$$X_k = \sum_{n=0}^{N-1} x_n \exp(-j\frac{2\pi nk}{N}), k = 0,1,\ldots N-1 \tag{1.1}$$

The DFT preserves energy within a factor 1/N:

$$\sum_{n=0}^{N-1} x_n x_n^* = \frac{1}{N}\sum_{k=0}^{N-1} X_k X_k^* \tag{1.2}$$

and the N-term sequence $\{|X_0|^2, |X_1|^2, \ldots, |X_{N-1}|^2\}$ is called periodogram of the sequence

$\{x_0, x_1, ..., x_{N-1}\}$. However, this sequence doesn't bear enough information to be called discrete energy spectrum. This can only obtain data for all $f < \frac{1}{2\Delta t}$, where Δt is the sampling period. If the energy spectrum $|X(f)|^2$ is desired, $X(f)$ must be known at frequencies that are at least twice as more finely spaced. This is due to the fact that $|X(f)|^2$ is the Fourier transform of the autocorrelation function of x(t), which is clearly twice as wide as x(t). Therefore, one has to append N-1 zeroes to the N+1 sequence $\{x(0), x(\Delta t), ..., x(N\Delta t)\}$ as in linear autocorrelation. Hence, it is possible to define the discrete energy spectrum of $\{x(0), x(\Delta t), ..., x(N\Delta t)\}$ as the periodogram E_k of the 2N-term sequence $\{x(0), x(\Delta t), ..., x(N\Delta t), 0, 0, ..., 0\}$:

$$E_k = \left| \sum_{n=0}^{N} x(n\Delta t) W^{\frac{nk}{2}} \right|^2, k = 0, 1, ..., 2N-1 \tag{1.3}$$

1.2 Thesis Outline

This section provides an overview of the material discussed in this thesis. In the present chapter, previous work on the large displacement actuators, microtribology and various lubrication methods and frequency domain measurement are presented as background for the work presented in this thesis. The motivations for low-cost large displacement actuators used as optical fiber switch and the great stability requirement of the switch are discussed. Finally, the work done for this thesis is summarized.

Chapter 2 presents design principle of the large displacement actuator, composed of a comb drive and a rack-pinion design. The mechanical parameters of the comb drive and constraints are addressed. The electrical analysis, including lateral displacement and

vertical levitation mechanisms, fringing effect which helps to actuate the comb drive and the equivalent circuit are discussed. The concept of "Balanced Comb Drive" to suppress rotation is proposed. Finite element method analysis using COSMOSEMS for electrostatic analysis and ANSYS for modal analysis are demonstrated.

Chapter 3 presents the fabrication of the device with a surface micromachining process – Multi-User MEMS Process (MUMPs). Process parameters and device geometry are provided in details. The device layout, 3-dimension view and cross-sections are illustrated. The design optimization is also discussed. The results of the fabrication and lubrication are then presented.

Measurement methods in order to separate the motional current from the feedthrough in the spectrum are discussed in details in chapter 4. Circuit configuration and its function are presented. Theoretical formula governing the spectrum is derived and analyzed. Plots of the spectrum using Matlab are demonstrated.

The experimental results of this thesis are presented in chapter 5. Two kinds of experimental data, in time domain and frequency domain are collected. Test setup of probe station, bonding machine and scanning electron microscopy are addressed. The SEM observations and spectrum analysis both shows balanced comb drive has superior stability over the unbalanced comb drive. The theoretical formula derived in chapter 4 are experimentally verified. Failure modes and possible reasons are discussed.

Chapter 6 gives a conclusion of the design, theoretical analysis and experimental results presented in the thesis and a brief discussion of future work that could be based on

this device.

1.3 Summary of the Work of this thesis

- Literature review, feasibility research and design of MEMS device.
- Theoretical analysis of mechanical properties and electrical properties.
- Finite element simulation using ANSYS of the resonant modes and the system model, while is verified using MATLAB.
- Finite element simulation using COSMOSEMS, illustrates the lateral resonant mechanism, vertical levitation and fringing effect.
- Derivative of theoretic formulas in frequency domain for mixing frequency measurement and frequency doubling measurement.
- Layout using Cadence, bonding and application of lubricant.
- Experiments in time domain in probe station and SEM. Experiments in frequency domain in atmosphere and vacuum.
- Comparison of theoretical analysis and experiment data, draw conclusion

CHAPTER 2 DESIGN PRINCIPLE

2.1 Design Principle

In order to realize the large lateral displacement actuation, a comb drive, which can reach displacement as large as 10 μm according to publications, is used as power source. A gear system is used to transfer the lateral displacement to rotational displacement, through a cantilever beam attached to the comb drive. There is a beam attached to the gear system, the tip of which is designed for optical switching. A layer of gold is deposited on the beam for two reasons: the different surface stress between gold and polysilicon will induce the beam to buckle upward; the smooth surface of gold is perfect for reflection and can be used as a mirror. The figure 2.1 shows the device layout.

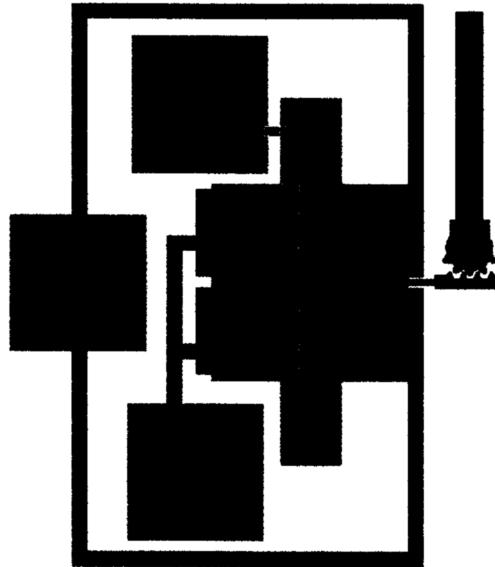

Figure 2.1: CADENCE layout of large lateral displacement actuator

When a proper voltage configuration is applied to the comb drive, because of the electrostatic drive force between the fixed fingers and movable fingers, and the restoring force of the springs, the comb drive will move back and forth. When the AC

frequency reaches the mechanical resonant frequency of the springs, the displacement will reach the maximum. A comb drive with 200 μm-long, 2 μm-wide springs and 2 μm gap between fingers, can reach 10 μm displacement at its resonant frequency, which is around 18kHz depending on the device parameters and microfabrication parameters, for example, Young's Modulus and surface stress.

The rack is driven by the comb drive, and at the same time, transfering the linear motion to rotation rotary motion though the pinion. The teeth are designed according to mechanical theory and MUMPs design rule, and the rotary motion is simulated to make sure that the motion will not be blocked due to bad design of teeth, as shown in figure 2.2. It also shows that, the pinion rotates 7 degree for the first 5 μm displacement of the rack, and 12 degree per 5 μm displacement later.

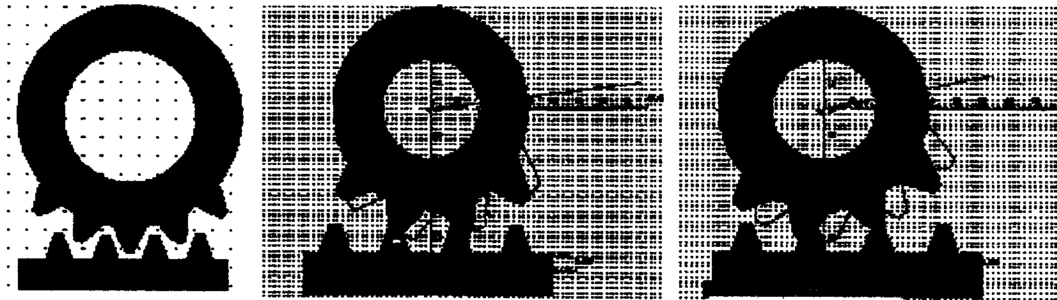

Figure 2.2: a) the original gear system without displacement b) the rack moves 5 μm to the right, the pinion rotates 7 degrees, as shown in the outline. c) The rack moves another 5 μm; the pinion will rotate another 12 degrees. In both situations, the rack and pinion will not block. In this design, the inner radius is 10 μm and the outer radius is 20 μm. Thus according to the figure, the pinion rotates 19 degree totally for 10 μm displacement

When a long beam is attached to the pinion, the displacement at the tip of the beam will be approximately the product of beam length and the sine of the rotation angle. In the case of figure 2.2, if a 100 μm-long beam is attached, the displacement at the tip will be around 30 μm for 10 μm lateral displacement.

2.1.1 Comb Drive Design

The common feature of comb drive used as power source is that its resonant

mode should be linear. The designers should explicitly choose mechanical geometries that preclude rotational motion. The folded- beam suspension can effectively suppress vertical vibration and rotational motion by high stiffness ratios. However, when a cantilever beam is attached to the moving plate at one side, perpendicular to the length of folded springs, as shown in figure 1.1 and figure 1.2, the geometry is not symmetric and the system is susceptible to rotational motions. Deliberate considerations are necessary to maintain the system rotational equilibrium, in another word, to maintain torque balance. The simplest design is "balanced comb drive", attaching a beam with the same shape and mass to the other side.

In order to compare the properties of the balanced and unbalanced comb drives, these two kinds of power source are designed with the same parameters. Detailed design considerations, mechanical analysis and electrical analysis could be found in 2.2 and 2.3.

2.1.2 Rack and Pinion Design

Gear teeth are used to provide a non-slip drive when the motion is to be transmitted from one shaft to another. The shape and size of the teeth become critical when the motion should be transmitted smoothly. The contacting cam surface on the mating gears must have the following properties [33]:

1. Continuity of action: the height and the lengthwise shape of the active profiles of the teeth must be such that, before one pair of teeth goes out of contact during mesh, a second pair will have picked up its share of the load.
2. The spacing between the successive teeth must be such that a second pair of tooth-contacting surfaces is in the proper positions to receive the load before the first leave mesh.

3. The shape of the contacting surfaces of the teeth must be such that the angular velocity of the driving member of the pair is smoothly imparted to the driven member in the proper ratio. The most widely used profile shape for active profiles of spur and helical gears that meets these requirements is the involute curve. This is called "conjugate action".

Here in the thesis, the most common profile, involute gear profiles, is used. On an involute profile gear tooth, the contact point starts closer to one gear, and as the gear spins, the contact point moves away from that gear and toward the other. It will describe a straight line that starts near one gear and ends up near the other. As the teeth first start to engage, the top gear tooth contacts the bottom gear tooth inside the pitch diameter. As the gear turns, the contact point slides up onto the thicker part of the top gear tooth. This pushes the top gear ahead, so it compensates for the slightly smaller gear tooth. As the gear continues to rotate, the contact point moves even further away, as shown in figure 2.3. Even though the contact point diameter changes continually, the speed remains the same, producing a constant ratio of rotational speed.

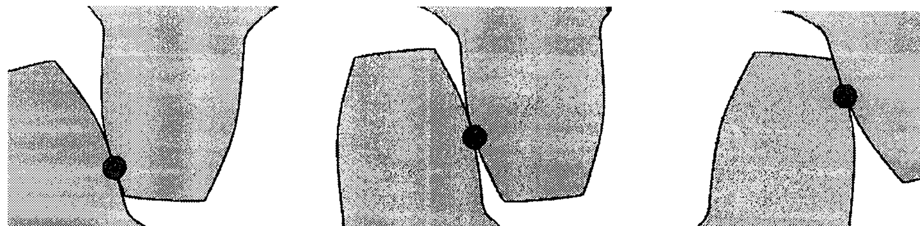

Figure 2.3: The contact point of involute gear

Rack and pinion gears can used to convert rotation into linear motion. A perfect example of this is the steering system on cars. The steering wheel rotates a gear, which engages the rack. As the gear turns, it slides the rack either to the right or left, depends on which way you turn the wheel.

However, small modifications should be considered when applying the mechanical principles into microfabrication, due to well-defined design rules and

fabrication limitations. First of all, the minimum feature for poly1 layer in POLYMUMPs is $2\,\mu m$, which means that there will be at least $2\,\mu m$-gap between the teeth at the initial state. When the gear chain begins to rotate and every time it changes rotate direction, it has to overcome the $2\,\mu m$ distance before transferring the motion. Besides, the rule "POLY1 space to ANCHOR2" defines the gap between the hub and the gear, which means the gap is at least $3\,\mu m$. This gap differs from the one in mechanical gears in real life in two ways, first, the gap is relatively large compared with the gear and the hub; second, there is no efficient lubricants to fill in the gap.

Secondly, the masks in POLYMUMPs are printed with a $0.25\,\mu m$ spot size, therefore this limits all features. When the structure doesn't adhere to the $0.25\,\mu m$ grid, the objects will snap to a $0.25\,\mu m$ grid. The objects maybe slightly bigger or smaller then expected. The shape of the teeth may change slightly due to the spot size. This means the actual shape of the teeth cannot be involute profile.

Thirdly, special consideration of the functionality is necessary. When the rack transfers the motion to the gear, a downward force on the rack is generated and may cause the gear run out of mesh. Slide proof support should be provided. Special designed slide proof support to reduce the friction is shown in figure 2.4. A stop anchor on the right is to prevent the rack and gear run out of mesh. The cross-section of the gear is also shown in figure 2.4.b. The substrate is covered by a layer of silicon nitride. Poly1 is used to form the gear and the teeth, which are supported by dimples. The size of the hub is defined by ANCHOR2, and poly2 is deposited to form the hub.

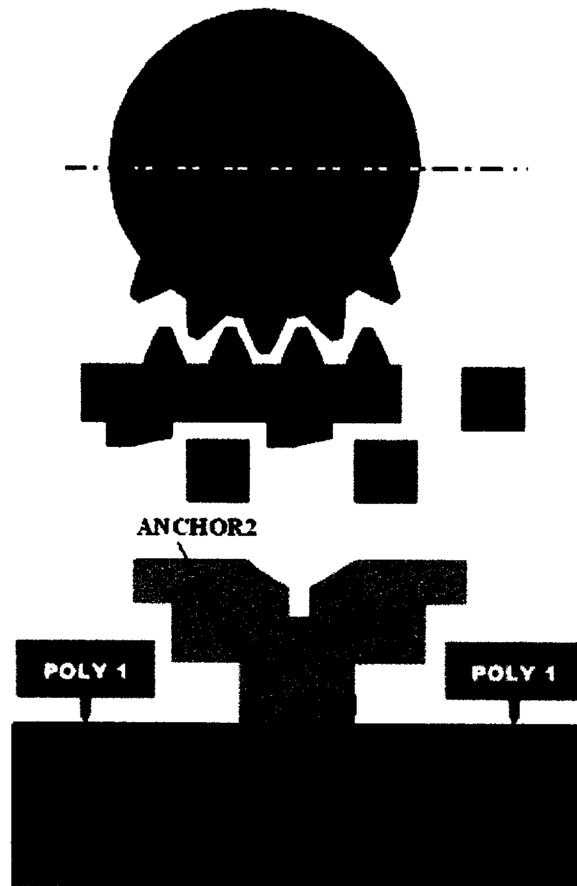

Figure 2.4: a) the layout of rack and pinion, with slide proof support underneath and stop anchor on the right; b) the cross-section of the gear

The three requirements of the gear teeth are verified by modeling the motion of the rack and pinion, as shown in figure 2.5. In this design, the inner radius of poly1 is 10 μm and the outer radius is 20 μm. In figure 2.5.a, the rack moves 5 μm to the right, and the gear rotates 7 degree. For the first 2 μm, the rack overcomes the gap between the teeth, and for the 3 μm afterward, the rack rotates the gear. In figure 2.5.b, the rack moves another 5 μm and the gear rotates 12 degree. In this modeling, the continuity of action and conjugate action are fully satisfied. But when the direction of motion changes, the rack has to move around 4 μm in order to overcome the gap. This discontinuity comes from the limitation of the design rule.

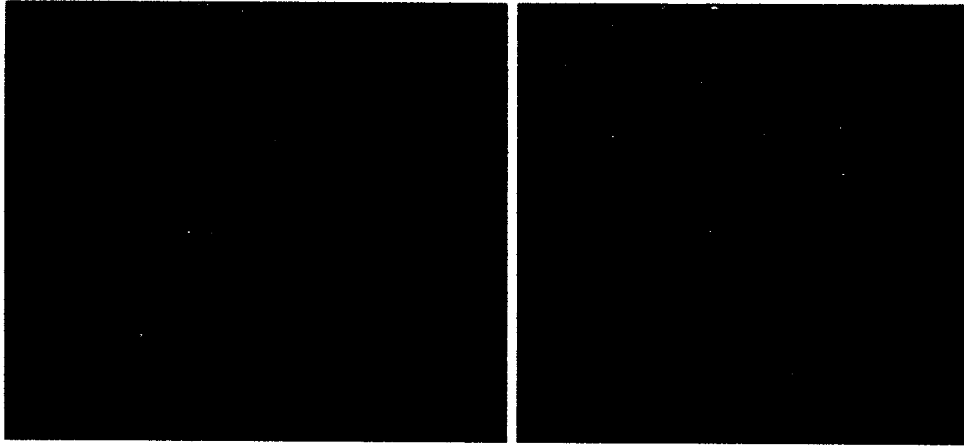

a) *b)*
Figure 2.5: The modeling of the rack and pinion motion

2.2 Comb Drive Mechanical Analysis

In this section, a mechanical analysis for both the lateral and vertical spring constants, together with the resulting effects, like resonant frequency, quality factor Q, and vertical levitation will be illustrated. Simulation using finite element analysis will be discussed. Design optimization according to the simulation result will be presented. Finally a system model will be presented.

2.2.1 Resonant frequency:

The folded beam suspension has two advantages: first, it allows the relief of the built-in stress of the structural polysilicon film as well as axial stress induced by large vibrational amplitude; secondly, the spring constant along the y direction is much higher than that along the x direction [6]. The center anchors allow the parallel beams to expand or contract in the y direction, relieving most of the built-in and induced stress.

The ideal mode shape of a folded beam support at resonant frequency is shown in figure 2.6 [6]. The structure is statically displaced by a distance of X_0 under an applied force F_x in the positive x direction. Assuming the outer connecting truss for

the four beam segments is rigid, which is justified because of its wider design, the slopes at both ends of the beams are zero. Under all these ideal conditions, the lateral spring constant and vertical spring constant can be expressed as:

$$K_x = \frac{2EhW^3}{L^3} \qquad K_z = \frac{2EWh^3}{L^3} \tag{2.1}$$

Where E is the Young's modulus, h is the thickness of the structural polysilicon layer, w is the width of the beam, and L is the length of the beam. The system spring constant in the y direction to that in the x direction is more than 10000 if L=200 μm and w=2 μm. The motion in the y direction is very unlikely.

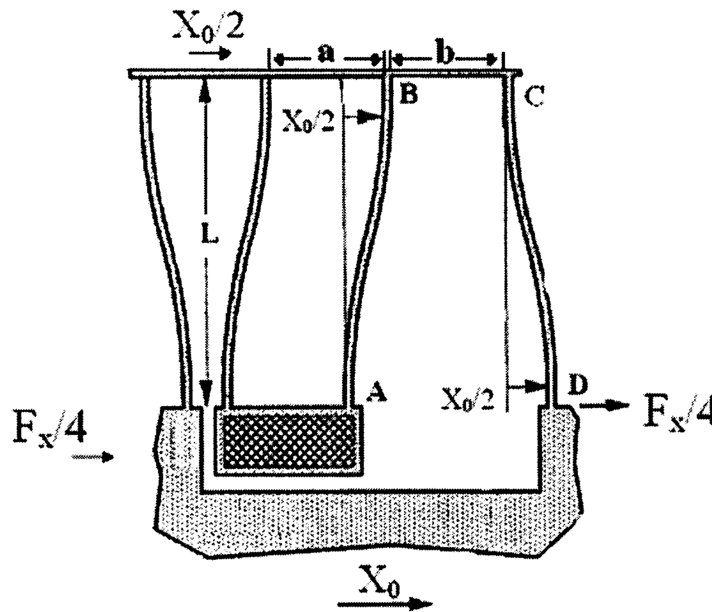

Figure 2.6: Mode shape of a folded beam support when the resonant plate is displaced by X_0 under a force of F_x [6]

The fundamental lateral resonant frequency of the folded beam system can be evaluated by Rayleigh's energy method. This method equates the maximum potential energy to the maximum kinetic energy, assuming the motion to be harmonic and the mode shapes are associated with the static deflections of the various beams due to unit forces applied to the comb. Thus the resonant frequency is given by the

expression:

$$f_0 = \frac{1}{2\pi}\left[\frac{k_x}{M_{eff}}\right]^{\frac{1}{2}} = \frac{1}{2\pi}\left[\frac{2Eh(W/L)^3}{M_p + \frac{1}{4}M_t + \frac{12}{35}M_b}\right]^{\frac{1}{2}} \tag{2.2}$$

Where M_p is the shuttle mass, M_t is the total combined mass of folding trusses; M_b is the total combined mass of the suspending beams. The fundamental resonant frequency depends on materials properties and geometry.

The nominal undamped lateral in-plane resonant modes and resonant frequencies under ideal conformal deposition, without confining the outer combining truss, can also be determined by 3-D finite element modeling tool like ANSYS. Figure 2.7 is the first three modes of a standard comb drive simulated using ANSYS, while the red parts show the largest displacement and the blue parts represent zero displacement.

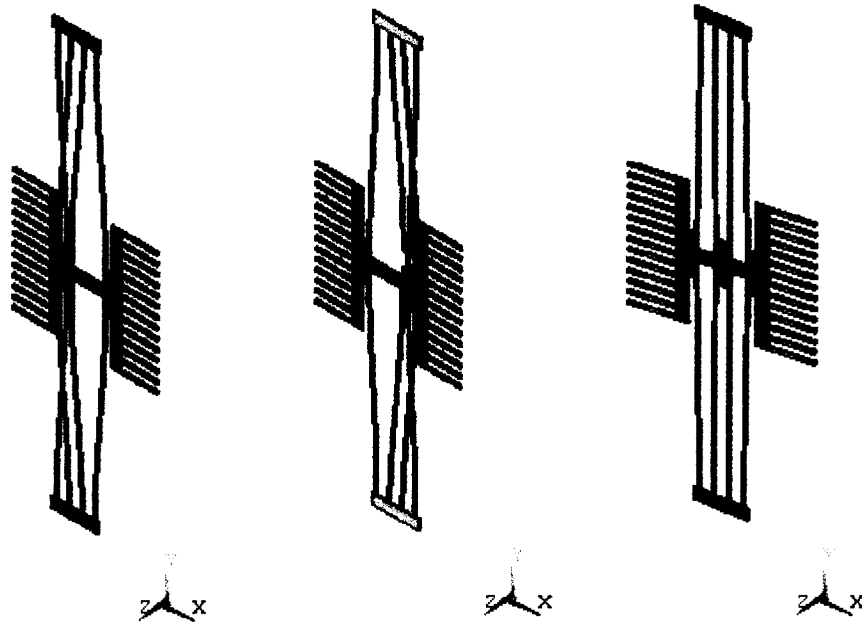

Figure 2.7: The first three resonant modes of standard comb drive : a) lateral resonance; b) vertical resonance; c) rotational resonance

Balanced comb drive behaves exactly like the standard comb drives. The

first three resonant modes are shown in figure 2.8. The lateral resonant frequency can be calculated from equation (2.2).

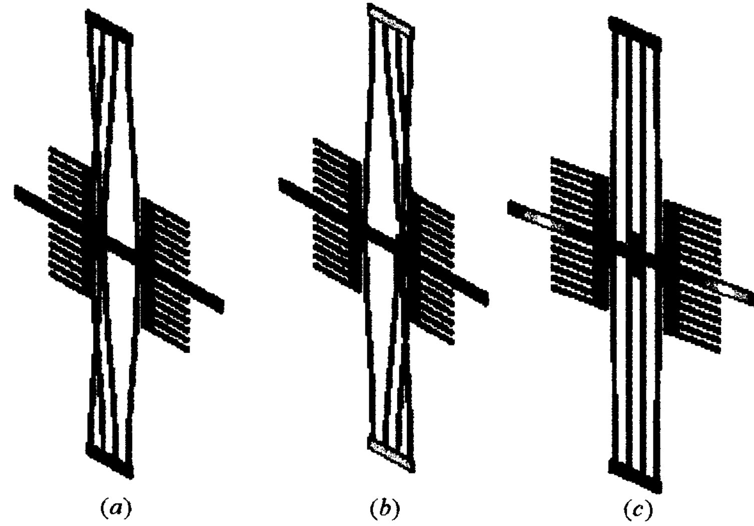

Figure 2.8: The displacement contour plots of the first three resonant modes of the balanced design: a) the lateral resonant mode; b) the vertical resonant mode and c) the rotational resonant mode

TABLE 2.1: Unbalanced Comb Drive Parameters and geometry parameters

Parameter	**Value**	**Parameter**	**Value**
Finger Length	40 μm	Structural Layer Thickness	2 μm
Folded-Beam Width	2 μm	Folded-Beam Length	200 μm
Finger Width	3 μm	Finger Gap Spacing	3 μm
No. of Fingers, left, right	14, 12	Width of Cantilever Beam	15 μm
Young's Modulus [34]	160-180Gpa	Length of Cantilever Beam	80 μm
Effective Mass	$5.4568\times10^{-11}kg$	Finger engagement	20 μm
System Spring Constant	$0.62N/m$	Predicted Resonant Frequency	16964 Hz

However for unbalanced comb drives, rotational resonant modes are not fully suppressed, and the resonant modes should be determined using sophisticated programs such as ANSYS. Table 2.1 lists the fabricated unbalanced comb drive parameters used for SEM observation, in which the effective mass is calculated under

the assumption that there is no offset and sidewall angle of polysilicon devices fabricated by the Multi-User MEMS Processes. The resonant frequency without the effect of process offset is calculated by equation 2.2, choosing 160Gps as Young's modulus. The resonant frequencies, including the effects of a distributed mass, residual stress and compliant support could be developed by the analytical model proposed in [20]. The simulated lateral resonant mode shape through ANSYS is shown in figure 2.9. The displacement contour plot in Z direction (perpendicular to the substrate) at lateral resonant mode indicates the rotation due to the asymmetry. The resonant frequency is a little bit higher than the predicted one because of the asymmetry.

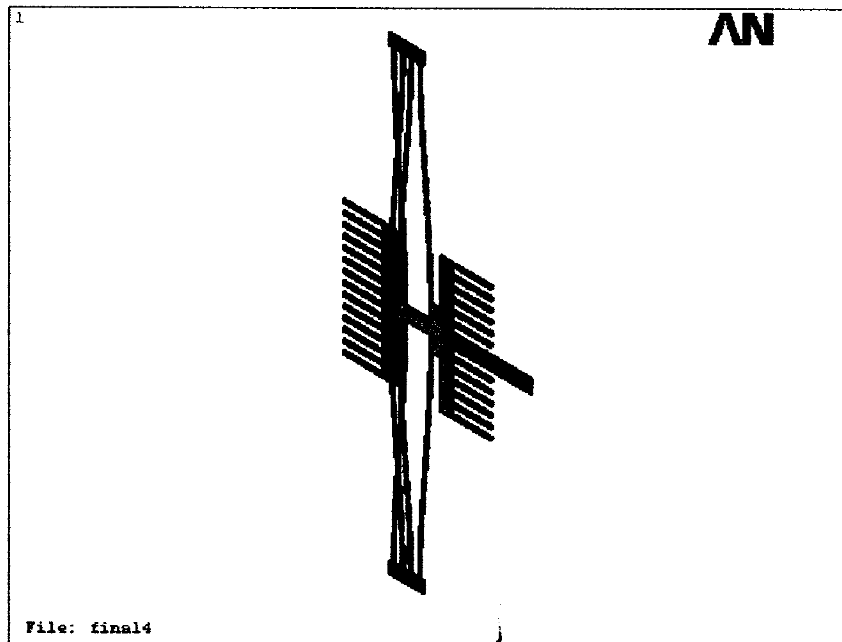

Figure 2.9 Displacement contour plot in Z direction at lateral resonant mode

2.2.2 Slide Film Damping

In the laterally driven microstructures, the damping level determines their amplitude response and stability [35] and viscous drag of the ambient fluid is the

amplitude response and stability [35] and viscous drag of the ambient fluid is the dominant dissipative source. Therefore damping is a crucial parameter to the device's functionality.

Slide film damping occurs if two surfaces separated by a thin fluid film move tangentially with respect to each other and energy is dissipated due to the viscous flow. In the comb-drive system, the damping mechanism includes slide-film damping force on the bottom, slide film damping on top, slide film damping of the sidewalls and air drag force. There are two kinds of slide film damping depending on the working frequency. Couette flow assumes a constant velocity gradient across the fluid gap and tangentially moving surfaces at low frequencies produce a nearly constant velocity gradient in the fluid, so the Couette flow is applicable to low frequency. Stokes flow assumes that the velocity gradient is not constant across the fluid gap. Tangentially moving surfaces at high frequencies do not produce a constant velocity gradient, so the Stokes flow is applicable to high frequencies. The transition from Couette to Stokes flow occurs near the cut-off frequency, which is given in equation 2.3:

$$f_c = \frac{\eta}{2\pi\rho d^2} \tag{2.3}$$

where ρ is the fluid density and η is the dynamic viscosity and d is the gap separation. In the case of air as the fluid, the density is 1.2kg/m^3 and the dynamic viscosity is 17.4x10^{-6}Pa·s, thus the cut-off frequency is 2.3x10^{6}Hz, which is much higher than the operating frequency of comb drive. So the major damping effect in comb drive system is Couette damping.

The damping force of Couette flow type can be expressed as:

$$F_d = \frac{\eta A_{eff}}{d}\frac{dx}{dt} = c\frac{dx}{dt} \tag{2.4}$$

$$A_{eff} = A_p + \frac{1}{4} A_t + \frac{12}{35} A_b \qquad (2.5)$$

where c is the damping coefficient, A_{eff} is the effective area, A_p is the plate area, A_t is the truss area, A_b is the beam area, d is the separation and η is the air dynamic viscosity. The damping force is proportional to the velocity. This is usually the most important force component among all the damping force components.

2.2.3 Quality factor Q

There are several dissipative processes during lateral motion, such as Couette flow underneath the plate, air drag on the top surface, direct air resistance related to the thickness of the structure and damping in the comb gaps. All these damping process affect the quality factor Q, but energy dissipation of Couette flow is dominant in the small gap between the suspended structure and the substrate.

The lateral quality factor Q is estimated by assuming that Couette flow underneath the plate is the dominant dissipative process. In this case, Q can be calculated as:

$$Q = \frac{d}{\mu A_q}(MK_{sys})^{\frac{1}{2}} = \frac{dk}{2\pi f_r \mu A_q} \qquad (2.6)$$

where μ is the absolute viscosity of air ($1.8*10^{-5}$ N sm^{-2}), A_p is the damping-related effective area of the system, given by $A_q = A_p + 0.5(A_t + A_b)$, and d is the offset between the plate and the substrate [35]. One of the advantages of the lateral resonant structures is that the quality factor in the lateral direction is much higher than that in the motion normal to the substrate. Thus when operating in air, the vertical motion is effectively restrained.

The second main damping factor comes from the small gap between the fingers. In the previous work of William Tang [36], the relation between finger gap

and quality factor is demonstrated. The Q is low for structures with either small finger gaps or widely separated fingers. For a set of 12 finger ($20\,\mu m \times 2\,\mu m \times 2\,\mu m$) test structures with different finger gaps, the quality factor Q at atmosphere pressure reaches maximum around 32 when the finger gap equals to 3.

The quality factor Q can be also deduced from the –3dB bandwidth using the following formula:

$$Q = \frac{f_r}{f_2 - f_1} \tag{2.7}$$

where f_r is the lateral resonant frequency and $f_2 - f_1$ is the –3dB bandwidth. The resonant frequency can be determined by continuously changing the output frequency until the blur envelop of the vibrating structure observed through the eyepieces or the video of SEM reaches a maximum. While the –3dB bandwidth can be estimated by running the output frequency away from resonance, until the blur envelop decreases to roughly 70% of the maximum, as shown in figure 2.10.

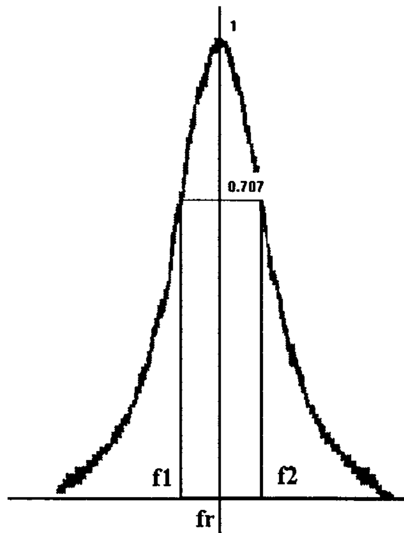

Figure 2.10: Q can be determined through the resonant frequency and the –3dB bandwidth

When the device is tested in vacuum, the air damping is almost eliminated;

the vibrational energy is mostly dissipated to the substrate through the anchors, friction between dimples and substrate. The quality factor could be more than 50 000 in vacuum.

2.2.4 Comb Drive System model

From Newton's law $\sum F = ma$, Hook's law $F = kx$ and the analysis of the damping force above, the system's motion can be derived easily by the second order differential equation:

$$M\frac{d^2x}{dt^2} + c\frac{dx}{dt} + k_x x = F_x(t) \tag{2.8}$$

where the M is the mass of the actuator, k_x is the spring constant, and c is the damping coefficient. The homogenous form of this second order differential equation is

$$M\frac{d^2x}{dt^2} + c\frac{dx}{dt} + k_x x = 0 \tag{2.9}$$

and the characteristic equation is:

$$\lambda^2 + \frac{c}{M}\lambda + \frac{k_x}{M} = 0 \tag{2.10}$$

and λ can be solved from this equation as:

$$\lambda_{1,2} = -\frac{c}{2M} \pm \left(\frac{c^2}{4M^2} - \frac{k}{M}\right)^{\frac{1}{2}} \tag{2.11}$$

We can distinguish three possible cases depending on the algebraic sign of $\frac{c^2}{4M^2} - \frac{k}{M}$. Since the solution will contain the damping factor $e^{-\frac{c}{2M}t}$ and $c/2M > 0$, the displacements of the mass will become negligible for large time.

When $\frac{c^2}{4M^2} - \frac{k}{M} > 0$, the system is overdamped. The system represents a

smooth and nonoscillatory motion. When $\frac{c^2}{4M^2}-\frac{k}{M}=0$, the system is said to be critically damped since any slight decrease in the damping force would result in oscillatory motion. The motion is quite similar to that of an overdamped system. When $\frac{c^2}{4M^2}-\frac{k}{M}<0$, the system is said to be underdamped since the damping coefficient is small compared to the spring constant. The motion is oscillatory, but because of the coefficient $e^{-\frac{c}{2M}t}$, the amplitude of vibration approaches 0 when time approaches infinite.

Whenever test in air or in vacuum, the comb drive system is underdamped. The item under the square root, $\frac{c^2}{4M^2}-\frac{k}{M}$, is less than zero and $\lambda_{1,2}$ should be imaginary. If we let $\frac{k}{M}=\omega_0{}^2$, $\frac{c}{2M}=\delta$ and $-\omega^2=\omega_0{}^2-\delta^2$, then the corresponding solution of (2.9) becomes:

$$x(t)=e^{-\delta t}\left[c_1\cos(\omega t)+c_2\sin(\omega t)\right] \tag{2.11}$$

where c_1 and c_2 can be determined by the boundary conditions. An under-damped system will behave similar to figure 2.11.

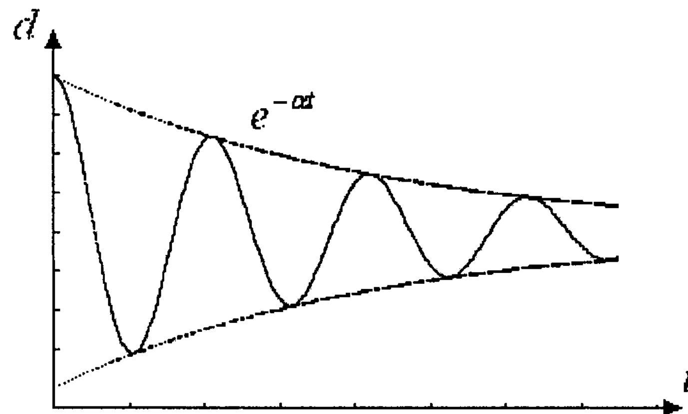

Figure 2.11: Viscous underdamped oscillation

Finite element simulation is carried out to show details of the comb system under electrical impulse stimulation. The geometry and material properties of the comb drive and the damping coefficient is listed in table 2.2.

Table 2.2: Geometry, material properties and damping coefficient used for simulation.

Length of finger	40 μm	Polysilicon density	$2.329*10^{-3}$ kg/ m3
Width of finger	2 μm	Effective mass	$5.4568*10^{-11}$kg
Thickness of structure layer	2 μm	Young's Modulus	150 Gpa
Overlap of fingers	20 μm	Poisson's ratio	0.22
Gap between fingers	3 μm	Spring constant	0.58 N/m
Length of spring	200 μm	Fluid density (air)	1.2 kg/ m^3
Width of spring	2 μm	Dynamic viscosity (air)	$17.4*10^{-6}$ Pa·s
Effective area	11715 μm^2	Damping coefficient	10^{-7}

The electromechanical system can be represented as a transducer, mass, spring and damper system. The system consists of an energy transducer (the comb drive), a spring structure, which is anchored to the substrate and provides restoring force to the system and a damping factor, as shown in figure 2.12. When the system is stimulated by a voltage impulse, the transducer transforms the electrical energy to damped mechanical vibration around its resonant frequency, which is determined by the spring constant and geometry.

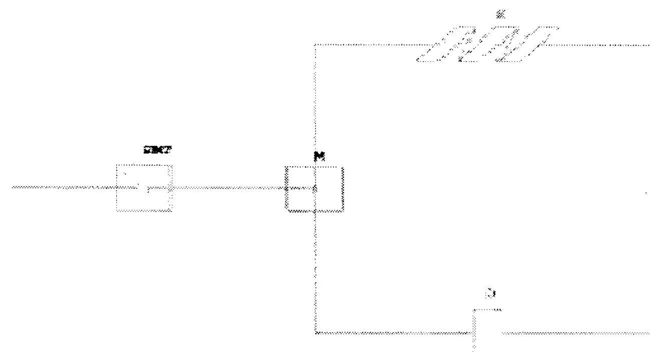

Figure 2.12: System model built with Ansys

The damping force is computed as

$$F_x = -c_v \frac{dx}{dt} \tag{2.12}$$

Where c_v is the damping coefficient given by $c_v=(c_v)_1 + (c_v)_2*v$, and v is the velocity. The second damping coefficient $(c_v)_2$ is to produce a nonlinear damping effect character of some fluid environments. If we consider the Couette damping only and neglect all the other damping mechanism, c_v can be expressed as:

$$c_v = \frac{\eta A}{d} = 1.0*10^{-7} \tag{2.13}$$

The spring constant is from the ANSYS simulation result, when 2uN is applied to the fingers on one side, the maximum displacement is 3.42micron, which result a spring constant of 0.58 N/m.

When t<0, the system is at steady state and the displacement equals to 0. At t=0, an electrical impulse of 50Volt is applied and the electrical energy transforms to mechanical vibration. The transducer reaches a maximum displacement of 0.7837 μm at $t=3*10^{-6}$s, where the voltage drops to zero. Then the system is operating under the effect of damping force and spring restoring force. Both the amplitude and frequency of the vibration decrease as time goes by. The displacement of the transducer is shown in figure 2.13.

The verification of the finite element method is carried out by solving the differential equation, assuming x(0)=0.7837 μm and $x(3e^{-5})$=0.7570 μm . These boundary conditions are taken from figure 2.13. The solution is plotted by Matlab, as shown in figure 2.14.

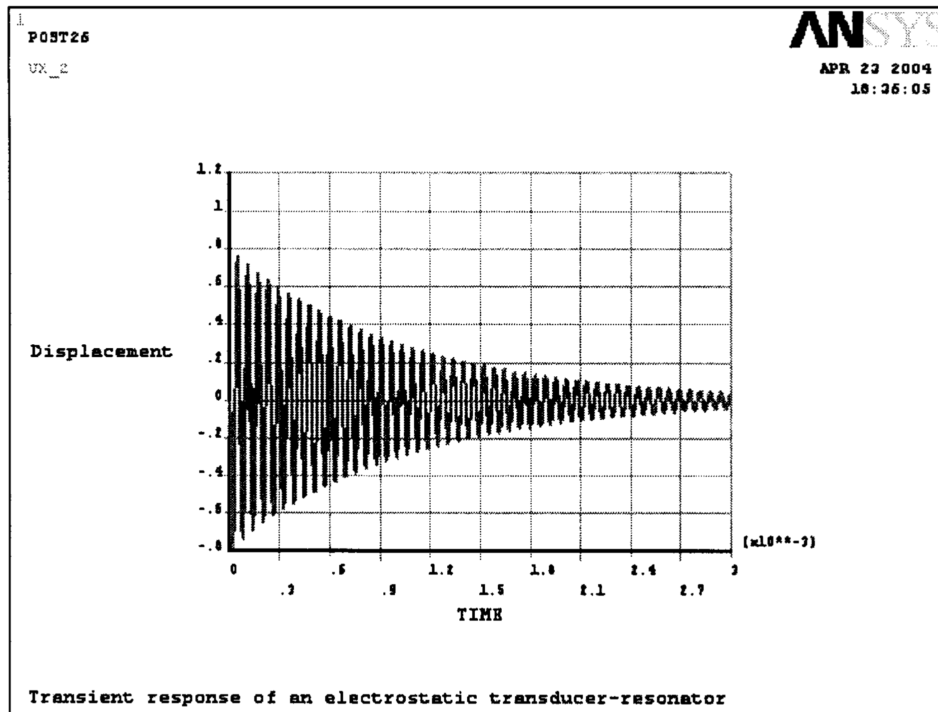

Figure 2.13: System reaction under electrical impulse stimulation. the impulse is 50v and lasts for $3*10^{-6}s$

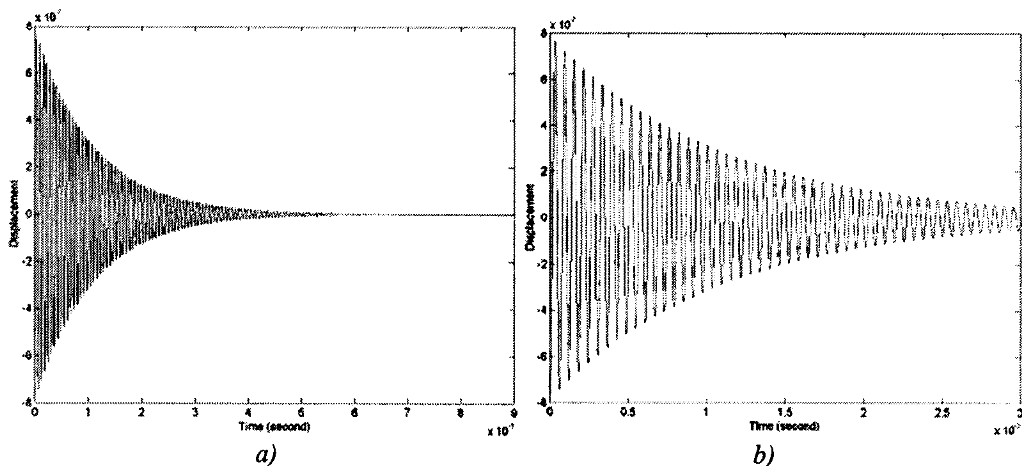

a) *b)*

Figure 2.14: Matlab verification, a) full time range, b) zoom in

In order to show the frequency component, the simulation result from ANSYS is process by MATLAB, using the DFT algorithm mentioned in 1.1.3. The discrete energy spectrum is shown in figure 2.15. The peak energy is around 18kHz as expected.

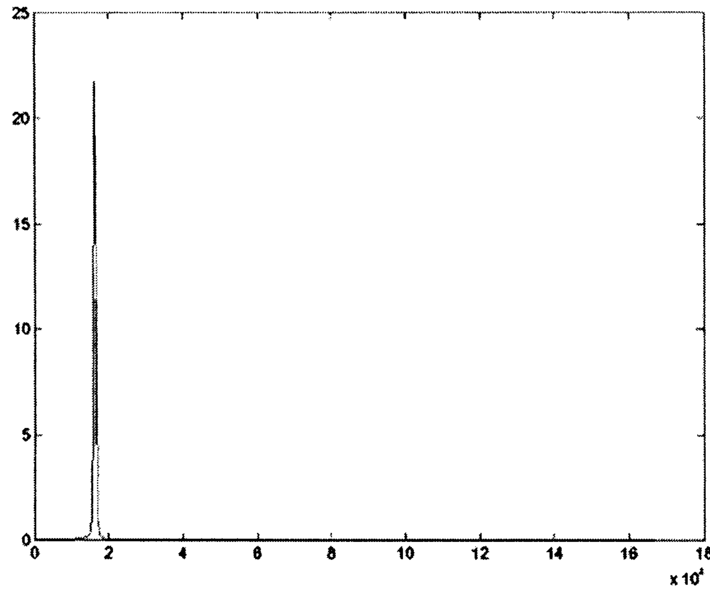

Figure2.15: Discrete energy spectrum of comb drive

2.3 Comb Drive Electrical Analysis

2.3.1 Lateral Displacement and Vertical Levitation Mechanism

The comb drive use electrostatic attraction to provide movement. The capacitance between the fixed fingers and movable fingers can be modeled by the parallel plate capacitor. According to the parallel plate capacitor theory, the capacitance of an ideal capacitor composed by the two adjacent plates can be determined by its area and separation:

$$C = \frac{Q}{V} = \frac{Q}{Ed} = \frac{Q}{\frac{\sigma}{\varepsilon_0}d} = \varepsilon_0 \frac{Q}{\frac{Q}{A}d} = \varepsilon_0 \frac{A}{d} \tag{2.14}$$

which shows that the capacitance is inversely proportional to d and proportional to the area of the plates. The above formulas are limited in that they do not account for fringe effects. In general, the effects of fringing for parallel plate capacitors can be neglected as long as both the width and height of the capacitor are significantly larger than the plate separation, a condition that is not true for comb drive. The fringing effects usually are not desired in sensor design because they cause non-linearity. But

fringing maybe useful in actuator designs in that it increases the electrostatic force/stiffness ratio [37]. When the thickness of the comb drive reduces towards the geometry limits, this ratio is no longer constant. And the capacitance will be larger than the ideal case of parallel plate model.

Electrostatic simulation using 3-D FEM (finite element method) software, COSMOSEMS, which takes fringe effect in to account, is carried out to elaborate the potential distribution and electrostatic field distribution. It provides insight into the mechanism of lateral displacement and the vertical levitation. Figure 2.16 is the analysis model used for simulation. The yellow box surrounding the structure is built to include a $10\,\mu m$-layer of air in the x, y and z directions and the air between finger gaps. The layout is built in Cadence and exported as .gds file, which can be imported by MEMSPro. The 3-D model is created by 3-D view generator in MEMSPro 3.0, but without the last step (sacrificial etching) in the process, in order to build the layer of air. Then the output .sat file is imported by COSMOSEMS for simulation.

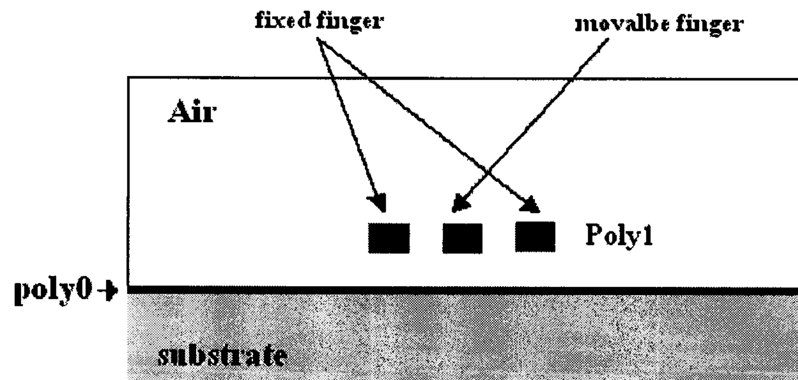

Figure 2.16: Electrostatic analysis model

First Order Finite Element Method, known as FOFEM is used here. This method is the simplest and most versatile methods for performing the electrostatic analysis. The electrode structure is surrounded by a boundary, on which the potential

distribution is assumed to be known. The region within the boundary is subdivided into coarse quadrilateral regions, whose sides are chosen to coincide with the electrode profiles. The coarse quadrilaterals are further subdivided to create a fine mesh. The mesh density can be varied as will, according to the accuracy required.

Then an electrostatic potential Φ_i is assigned to each mesh point. The potential is assumed to vary linearly with position inside each finite element. With this approximation, the potential everywhere inside an element is determined by the potentials at its nodes, and the potential throughout the entire space is determined by the set of potentials Φ_i (i=1,N) at the N mesh Points.

The potential distribution Φ_i (i=1,N) is now computed by minimizing the functional $F = \iiint_{vol} \frac{1}{2}\varepsilon \cdot \nabla\Phi \cdot \nabla\Phi dv$, subject to the prescribed boundary potential distribution. In this equation, Φ denotes the potential at a general point in the space, ε is the permittivity, dv is a volume element, and the integral is evaluated over the entire volume within the boundary. The expression $\varepsilon \cdot \nabla\Phi \cdot \nabla\Phi$ represents the energy density in the electric field, so the functional F represents the total energy stored in the field. Physically, the potential distribution adjusts itself so as to minimize the total stored energy. To minimize the functional numerically, the potentials Φ_i (i=1,N) are assigned to the mesh points, and the functional can then be expressed as a quadratic function of the mesh-point potentials. The requirement that the functional be minimized then yields a sparse set of linear "finite element equations." Each finite element equation related the potential at one mesh point to the potentials at the eight surrounding nodes. These equations can then be solved, by Gaussian elimination or by the incomplete Cholesky conjugate gradient method, to obtain the potential at each mesh point [38]. For extremely high accuracy, SOFEM may be used, but SOFEM

doesn't show many advantages for this case, because the profile of the comb drive doesn't contain any curvatures. In order to save processing time and storage space, FOFEM is used.

3-D model of two sets of fingers, appearing as solid lines in figure 2.17, surrounded by a 10-μm layer of air is built in MEMSPro. The structure's profile is: 2-μm -thick, 3-μm -wide and 40-μm -long fingers with 3-μm gap in between, 20-μm engagement and 2 μm offset above the 0.6-μm shielding. Figure 2.17 presents the front view of the potential distribution when the fixed fingers (left) are connected to ground and the movable fingers (right) are biased at 10 volts. Figure 2.18.a shows the front view electrical field vector plot. The electrical field and the positive charge on the movable structure yield an attractive force, which is the mechanism of the lateral displacement. The cross-section view is shown in figure 2.18.b. The top outlined rectangle in the middle is the 2-μm poly1 structural layer and the lower one is 0.6-μm poly0. The layer above poly1 is air. The upward electrical field and the positive charge on the movable fingers produce an upward electrostatic force, which is the mechanism of vertical levitation.

The levitation may cause the attached beam to deflect downward. If there is a pawl-ratchet mechanism or gear system at the other end of the beam, it might lead to disengagement. It is essential that both structures remain in the same plane. Special care should be taken to prevent the vertical levitation [7], [39].

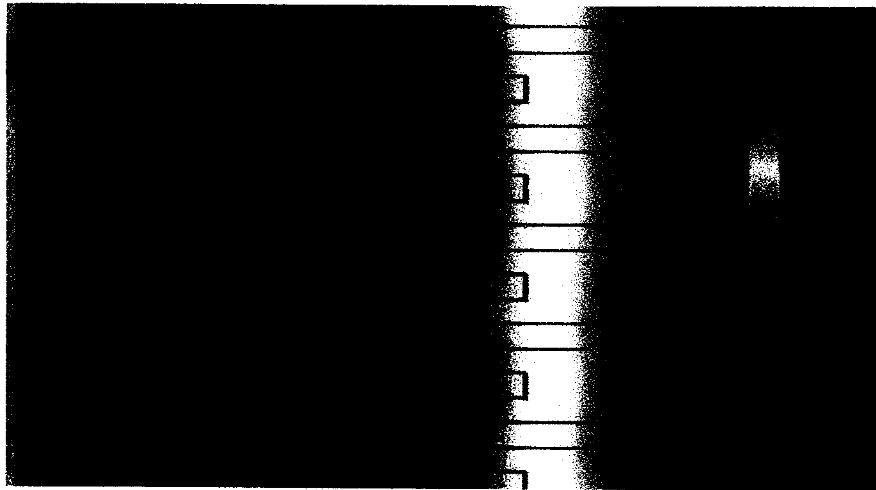

Figure 2.17: The potential distribution

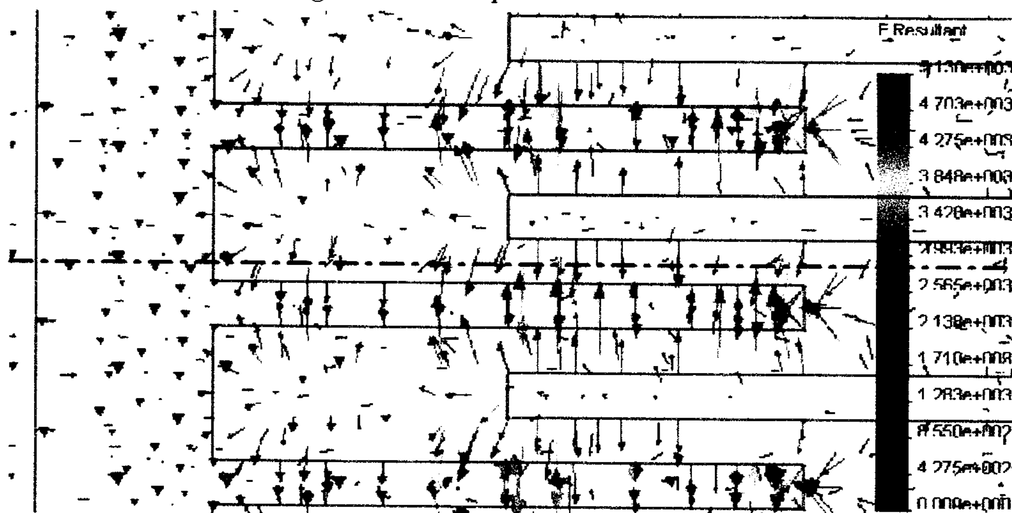

a)

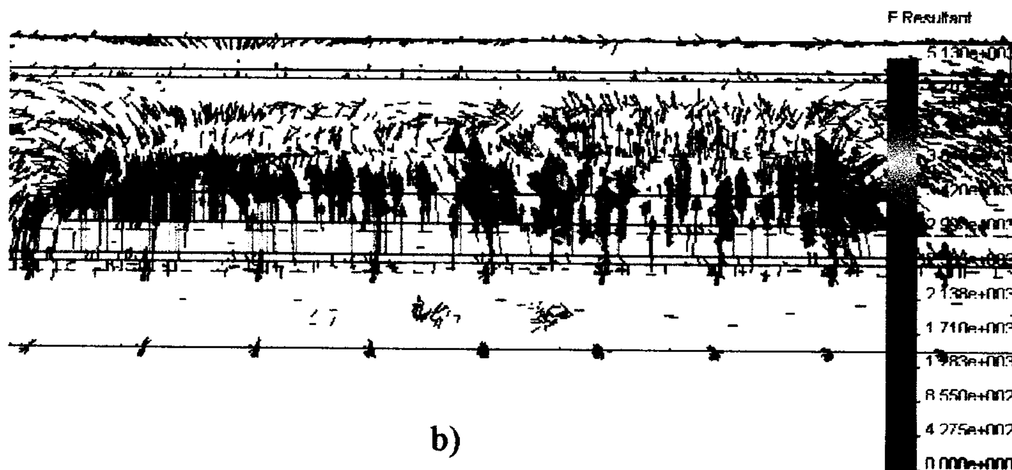

b)

Figure 2.18: The electrical field vector plot simulated using COSMOSEMS: a) front view; b) cross-section view

2.3.2 Fringing Effect

The fringing effect is clearly shown in figure 2.18 by the electrical field distribution outside the finger engagement. If we define ξ as a coefficient that models additional capacitance due to fringing, equal to the actual capacitance over the theoretical capacitance, then the simulation results in $\xi = 1.504$. The variation of the fringing constant versus the thickness of the polysilicon layer is shown in figure 2.19. As expected, the thicker the polysilicon is, the smaller fringing constant is.

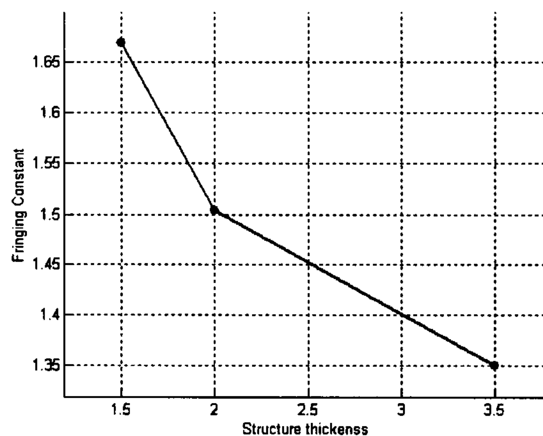

Figure 2.19: The variation of fringing constant versus structure thickness

2.3.3 Equivalent Circuit

Many different physical systems can be described by a linear second-order differential equation, similar to the differential equation of forced motion with damping. In order to develop the equivalent circuit of the comb drive, we will analysis the circuit elements, inductor, capacitor and resistor first.

The relationship of voltage drop and current in inductor, resistor and capacitor are shown in figure 2.20:

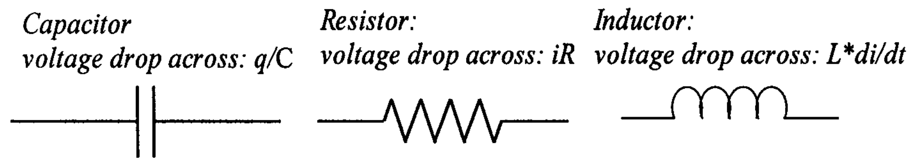

Figure 2.20: Circuit elements' electrical properties

If the L, C and R are connected in series, by Kirchhoff's second law, the sum of these voltages equals to the voltage impressed on the circuit:

$$L\frac{di}{dt}+Ri+\frac{1}{C}q=E(t) \tag{2.15}$$

and the charge on the capacitor is related to the current by:

$$i=\frac{dq}{dt} \tag{2.16}$$

so (2.5) becomes the linear second-order differential equation:

$$L\frac{d^2q}{dt^2}+R\frac{dq}{dt}+\frac{1}{C}q=E(t) \tag{2.17}$$

The system is overdamped, critically damped and underdamped depending on the relationship between R^2 and $\frac{4L}{C}$. The electrical vibrations of the L-C-R series circuit are quite similar to the forced vibration with damping $M\frac{d^2x}{dt^2}+c\frac{dx}{dt}+k_x x=F_x(t)$, and can be used as equivalent circuit to represent the comb drive system. L is similar to M , R is similar to c and $\frac{1}{C}$ is similar to k_x. If the electromechanical coupling coefficient η is defined as:

$$\eta=V_s\frac{\partial C}{\partial x} \tag{2.18}$$

then L , R and $\frac{1}{C}$ can be expressed as:

$$L = \frac{M}{\eta^2} \tag{2.19}$$

$$R = \frac{c}{\eta^2} = \frac{\sqrt{k_x M}}{Q\eta^2} \tag{2.20}$$

$$C = \frac{\eta^2}{k_x} \tag{2.21}$$

The parasitic feedthrough can be modeled by a capacitor in parallel with the L-C-R circuit, as shown in figure 2.21. C_p is the probe-to-probe feedthrough parasitic capacitance.

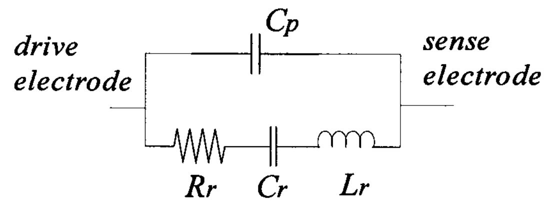

Figure 2.21: The equivalent circuit for the comb drive

CHAPTER 3: Fabrication and Post-processing

3.1 Design Implementation

The device fabrication using POLYMUMPs technology is provided by Cronos Integrated Microsystems, Inc. through Canadian Microelectronic Corporation (CMC). The Multi-User MEMS Process, known as POLYMUMPs technology, is a triple polysilicon, single metal surface micromachining process with silicon oxide (PSG) as the sacrificial material, and silicon nitride for electrical isolation from the highly conductive substrate [33]. Figure 3.1.a is a cross-sectional view of a micromotor fabricated using POLYMUMPs and figure 3.1.b is the released structure, which clearly shows the structural layer and the sacrificial layer. Since the POLYMUMPs is designed with the purpose of supporting many different designs on a single wafer, the thickness of the structural and sacrificial layers is fixed. Material layers, their thickness and lithography level names are listed in table 3.1.

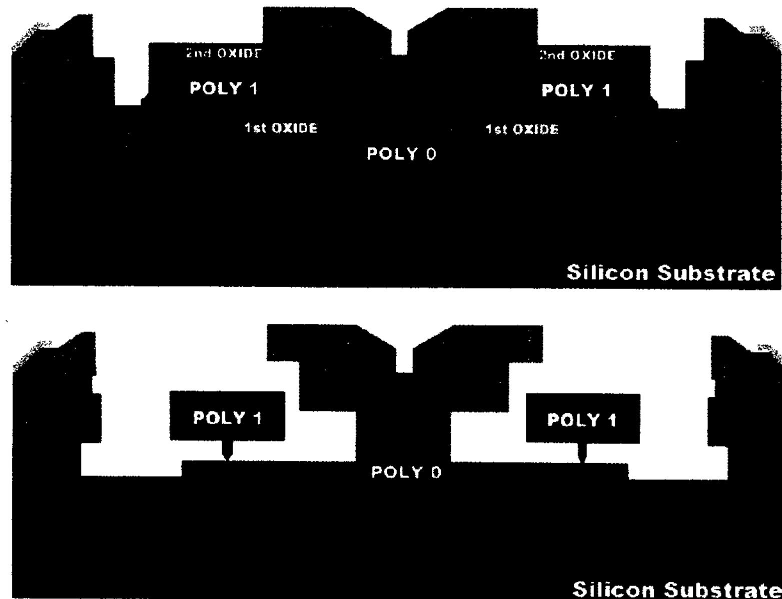

Figure 3.1: Cross-sectional view of a micromotor using POLYMUMPs, a) before releasing; b) after releasing [33]

Table 3.1: Layer names, thickness and lithography levels of POLYMUMPs [33]

Material Layer	Thickness	Lithography Level Name
Nitride	0.6 μm	---
Poly 0	0.5 μm	POLY0 (HOLE0)
First Oxide	2.0 μm	DIMPLE, ANCHOR1
Poly 1	2.0 μm	POLY1 (HOLE1)
Second Oxide	0.75 μm	POLY1_POLY2_VIA, ANCHOR2
Poly 2	1.5 μm	POLY2 (HOLE2)
Metal	0.5 μm	METAL (HOLEM)

The device in this fabrication can be divided into five categories, as described as follows:

1. Single side comb drive with an attached cantilever beam.
2. Unbalanced comb drive with an attached cantilever beam.
3. Unbalanced comb drive with microengine at the end of the cantilever beam.
4. Balanced comb drive with an attached cantilever beam.
5. Balanced comb drive with microengine at the end of the cantilever beam.

Each category contains different spring length, number of fingers, shape of shuttle and gear teeth shape for comparison.

3.2 Post-Processing

3.2.1 HF release

After the final layer, 0.5 μm metal layer which provides for probing, bonding, electrical routing and highly reflective mirror surface, is deposited and patterned using life-off, the unreleased structure is immersed in a bath of 49% HF for 1.5-2 minutes at room temperature. This is followed by several minutes in deionized water and then alcohol to reduce stiction, followed by at least 10 minutes in an oven at 110° C. However, even after alcohol rinse, device stiction is still a common

problem. One way to minimize this effect is to dry the chips after HF release by critical point drying in carbon dioxide. Considering the facility and experience, the HF release and carbon dioxide critical point drying are carried out by CMC.

Successful device release is verified by stimulation in probe station with a micromanipulator, as shown in figure 3.2. The displacement of the folded-beam is almost the same as the predicted one shown in figure 2.6. The release can also be verified in SEM by observation of the gap below POLY 1. In this case, the device should be tilted a large angle from horizontal.

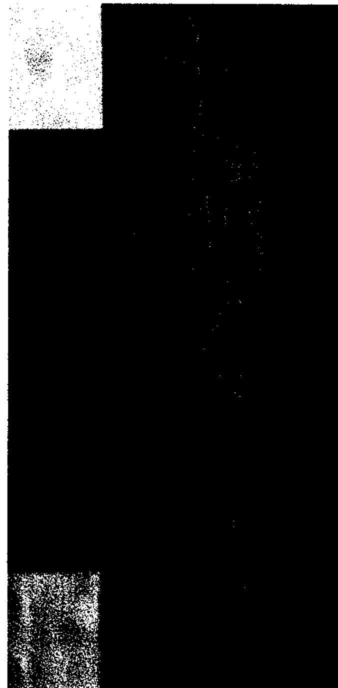

Figure 3.2: Stimulation of the device with a micromanipulator

Figure 3.3.a presents a device in the fifth category, the balanced comb drive with a microengine; b and c show different designs of gear teeth. The rotation of the gears shown indicates that the device is fully released. The rotation is due to fluidic force during the release process.

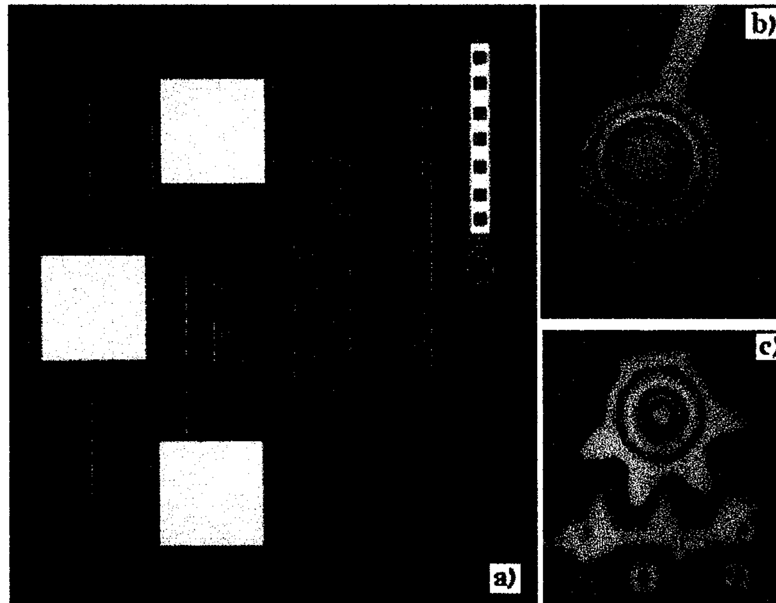

Figure 3.3: Microscope observations of the device. a) Large lateral displacement actuator; b)rotation due to fluidic force, small rotation angle leads to large displacement at the tip of the beam; c) different gear tooth design

3.2.2 Application of Lubricants

The relative magnitude of forces impacting the dynamics and performance of conventional macroscopic systems is quite different than that for MEMS. At the size scale of MEMS, gravitational forces become negligible. By far the most dominant forces at the microscale are associated with contacting or rubbing surfaces. Adhesion of contacting surface, named as "stiction" in chapter 1.1.2, and friction between sliding surfaces have the greatest impact on MEMS performance and reliability. There are several root causes that give rise to adhesion and friction-related failure.

In order to approximate de stiction, a simple comb drive, without dimples at the truss, as shown in figure 3.4 is fabricated. The length of the spring is 160 μm long and the width is 3 μm in order to generate relative large restoring force. The difference between this device and the other devices is there is no dimple at the end of

the folded-beam spring (truss). The device is support only by the dimples on the center cantilever beam. The experiment is carried out in probe station at atmosphere. A micromanipulator with three degrees of freedom driven by fine adjustment screws is used to stimulate the device. First the device is stimulated the same way as shown in figure 3.2 then the micromanipulator is withdrawn. Because of the large stiction force between poly1 and poly0, the central mass cannot move back with the restoring force of the springs. This experiment qualitatively shows the large friction, however, can not determine the stiction quantitatively. More advanced instruments, like atom force microscope (AFM) or friction force microscope can be used to calibrate the stiction.

One of the challenges of this design is to overcome the effect of stiction, which is mainly between the supporting dimples and the poly0, the hub and the gears, and the friction between the teeth. According to the POLYMUMPS FAQ [41], the surface roughness of poly0 after annealing is R_{rms}=12.12nm while R_{rms}=12.55nm for poly1. The stiction force between polysilicon layers at this surface roughness is not reported, but comparing the figures (friction and surface roughness) in [30], the stiction is large. The coefficient of static friction between polysilicon layers after annealing is characterized by M.G.Lim through a comb drive structure, which is between 3.9 and 5.9, much larger than that of polysilicon/silicon nitride contact (0.2-0.4), however, the result is much higher than expected [40], which may caused by the contaminants introduced by the ambient, including oxide buildup, dust particles, water vapor and other unknows in the environment. Optimization of design parameters and fabrication parameters may minimize the stiction. And application of lubricants may be useful for successful operation.

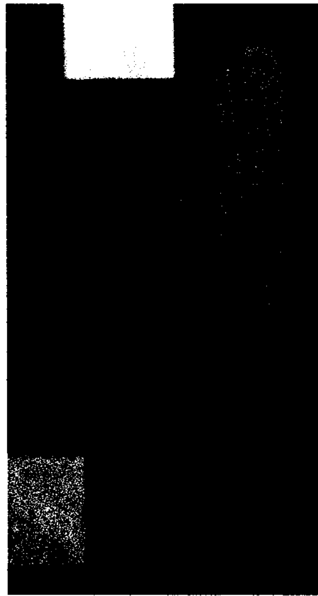

Figure 3.4: Observation of large friction between POLY1 and POLY0, when no supporting dimples at the ends of springs

Two kinds of lubricants will be used for comparison. Polar perfluoropolyether ($HO-CH_2-CF_2-O-(CF_2-CF_2-O)_m-(CF2-O)_n-CF_2-CH_2-OH$) (Fomblin PFPE Lubricant Z DOL 2000) is applied for test the effect of bonded lubricant. Baking at 150°C for an hour follows the naturally drying after the dip-coating technique, in order to obtain a bonded layer of lubricants. One nonpolar perfluoropolyether lubricant ($CF_3-O-CF_2-CF_2-O)_m-(CF2-O)_n-CF_3$) (Fomblin PFPE Lubricant Z 03) with low viscosity will be used to compare the result of bonded or unbonded polar lubricant. The less viscous lubricant gives a smaller critical film thickness because it is relatively easier to migrate to form menisci.

The lubrication is accomplished through a dip-coating technique. The device is vertically submerged into a breaker containing hydrocarbon solvent (Galden PFPE HT70) with 0.2% of the desired lubricant. Then the device is soaking for 5 to 10 minutes for different thickness and pulled out with a constant speed ranging from 0.5 to 6mm/s. Due to viscous force, a small amount of the solution was drawn up with

the moving device. The volatile solvent is quickly evaporated, leaving behind a lubricant film with even thickness on the device surface.

In order to conduct friction test on the same device with different lubricants, the lubricant removal for the non-polar lubricants was accomplished by sweeping a jet of a perfluorocarbon liquid. (Galden PFPE HT55) rapidly across the device surface while the device rotated at 4000rev/min. For the polar lubricant, an about 1nm thick lubricant was still left on the device surface after the use of this lubricant removal technique.

All these chemicals, Z DOL 2000, Z 03, HT55 and HT70 are all provided by SOLVAYSOLEXIS. The physical properties are listed in Table 3.2, 3.3 and 3.4.

Table 3.2: Available Grades and Typical Physical Properties of Fomblin PFPE Lubricant Z DOL 2000

Properties	Units	Z DOL 2000
Functional group	-	Alcohol
Appearance	Visual	Clear liquid
Molecular Weight	Amu	2000
Difunctional content	%	94
Kinematic viscosity	cSt	85
Density @ 20°C	g/ml	1.81
Vapor pressure @ 20°C	Torr	$2*10^{-5}$
Vapor pressure @ 100°C	Torr	$2*10^{-5}$
Surface tension @ 20°C	Dyne/cm	24

Table 3.3: Available Grades and Typical Physical Properties of Fomblin PFPE Lubricant Z 03

Properties	Units	Z 03
Appearance	Visual	Clear
Molecular weight	Amu	4000
Kinematic viscosity @ 20°C	cSt	30
Viscosity index(ASTM D2270)	-	317
Evaporation weight loss @ 149°C, 22hr	%	6.0

Surface tension @ 20°C	Dynes/cm	23
Density @ 20°C	g/cm³	1.82

Table 3.4: Available Grades and Typical Physical Properties of Galden PFPE HT55 and HT70

Typical Properties	Units	HT55	HT70
Boiling Point	°C	57	70
Pour Point	°C	<-110	<-110
Density, 25°C	g/cm³	1.65	1.68
Kinematic Viscosity, 25°C	cSt	0.45	0.50
Kinematic Viscosity, 0°C	cSt	0.64	0.75
Kinematic Viscosity, -20°C	cSt	0.91	1.09
Kinematic Viscosity, -40°C	cSt	1.40	1.79
Vapor Pressure, 25°C	torr	228	165
Heat of Vaporization @ Boiling Point	cal/g	22	17
Refractive Index, 25°C	—	1.280	1.280
Surface Tension, 25°C	dynes/cm	10	14
Average Molecular Weight	—	340	410
Dielectric Constant 25°C (1Khz)	—	1.86	1.86
Volume Resistivity	Ohm-cm	1×10^{15}	1×10^{15}

The effect of lubricants can be observed by the test device in category 1, the single side comb drive with an attached cantilever beam. The experiments are same as that shown in figure 3.4. After lubrication (bonded PFPE Z DOL 2000, unbonded PFPE Z DOL 2000, or PFPE Z 03), the device restores to the original position under the spring restoring force, which indicated a reduced stiction. All of the three lubricants are helpful to reduce stiction, and they are sent to wire bonding for further experiments, together with the chips without lubricant.

3.2.3 Bonding

In order to test the device in SEM chamber and for frequency analysis, wire bonding is carried out by West Bonding machine 7476E, as show in figure 3.5. Wire bonding provides electrical connection between the silicon chip and the external leads

of the semiconductor device using very fine wires. Two kinds of packages, DIP40 (dual in line) and CFP80 (ceramic quad flat pack) are used. Because of its small size, only CFP 80 is used in the SEM chamber.

During aluminum wedge bonding, a clamped wire is brought in contact with the bond pad. Ultrasonic energy is then applied to the wire for a specific duration while being held down by a specific amount of force, forming the first wedge bond between the wire and the bond pad. In fact, the bond scrubs against the bond pad, which cleans the bond pad of debris and oxides, exposing a fresh surface of the bond pad in the process. The wire is then run to the corresponding lead finger, against which it is again pressed. The second bond is again formed by applying ultrasonic energy to the wire. The wire is then broken off by clamping and movement of the wire. The wire specification and the parameter settings for the bonding machine are listed in table 3.5.

Table 3.5: Type of wire and parameter settings

Wire	Ultrasonic Time	Ultrasonic Power
99% Aluminum, 1%Silicon, diameter:25um Wires	30 ms	300

Figure 3.5 West Bond 7476E Wire Bonding machine

For the chips without application of lubricants, the bonding is successful. However, for the chips with lubricants (bonded or unbonded PFPE Z DOL 2000, or PFPE Z 03), it is very difficult to keep the wedge bond sticking to the chip. The "foreign material", the lubricants, together with the other contaminations such as unetched glass, silicon saw dust, process residues and oxide makes the bonding very difficult. Therefore, the chips with lubricants will not be used for further experiments.

CHAPTER 4 MEASUREMENT THEORY

When the mechanism of the lateral displacement, vertical levitation and the equivalent circuit are established, we now can proceed with the system behavior when the comb is driven by AC signals. The electrostatic comb can be driven from one side and sensed capacitively at the other side, by sensing the short circuit current through the time-varying interdigitated capacitor with a DC bias. Or alternatively the structure can be driven at two ports by AC signals that have 180° phase difference.

Both the driving force and the output current depend upon the variation in the comb capacitance C with the lateral displacement x. The key feature of the comb drive is the linearity of $\frac{\partial C}{\partial x}$ throughout the useful range of displacements. The electrostatic driving force is proportional to $\frac{\partial C}{\partial x}$ and can be expressed as:

$$\begin{aligned} F &= \frac{\xi}{2}\frac{\partial C}{\partial x}{v_D}^2 = \frac{\xi}{2}\frac{\partial C}{\partial x}(V_p + V_d \sin\omega_d t)^2 \\ &= \frac{\xi}{2}\frac{\partial C}{\partial x}(V_p^2 + \frac{1}{2}V_d^2 + 2V_pV_d\sin\omega_d t - \frac{1}{2}V_d^2\cos(2\omega_d t)) \end{aligned} \tag{4.1}$$

where v_D is the drive voltage across the movable fingers and driving electrode, V_p is the DC voltage applied to the shielding and the movable structure, and ξ is the fringing constant. Usually V_p is much larger than the signal V_d. According to equation 4.1, there is always a static force, which is proportional to ${V_p}^2$ which helps to stimulate the comb drive.

The current i_s at the sensing electrode related to the motion of the comb drive can be expressed as:

$$i_s = \frac{dQ}{dt} = \frac{d[\xi C v(t)]}{dt} = \xi C \frac{dv(t)}{dt} + \xi v(t) \frac{dC}{dx}\frac{dx}{dt} = i_c + i_m \tag{4.2}$$

where $v(t)$ is the voltage between the movable structure and the stationary sensing electrode. The first term on the right of the equation, i_c, is the capacitive current due to voltage change, the second term, i_m, is called motion induced current or motional current.

Another current component is the parasitic feedthrough current. This component comes from the parasitic capacitance between the pads, specifically the parasitic capacitance between POLY0 and highly conductive substrate, with silicon nitride in between. The relative permittivity of silicon nitride is $\varepsilon_r = 7.5$ and the thickness is $0.6\,\mu\text{m}$. According to the parallel plate theory, $C = \varepsilon_0 \frac{A}{d}$, the parasitic capacitance is much larger than the capacitance between fingers. And the parasitic current can be expressed as:

$$i_p = C_p \frac{dv}{dt} \tag{4.3}$$

Usually the feedthrough current is much larger than the capacitive current and motional current.

Unfortunately, the direct measurement of the motion current is difficult because of the relative large feedthrough current. In order to separate the useful current from the large parasitic current, a carrier signal must be used. The separation might also be achieved by frequency doubling with the input signal at half of the resonant frequency. And the second order electrostatic force in equation 4.1 will force the comb drive to resonant, and parasitic current at half of the resonant frequency is separated.

4.1 Frequency Doubling Measurement

As stated above, we might use frequency doubling to eliminate the effect of feedthrough, by applying a DC voltage, V_p, to the substrate and movable structure and one AC signal, $v_d(t)$, to the driving electrode.

At the drive port, the induced electrostatic force in the x direction, F_x, is given by equation 4.1. The electrostatic force now has three components at ω_d, $2\omega_d$ and DC. If $\omega_d = \frac{1}{2}\omega_r$, the resonance can be only excited by the frequency at $2\omega_d$, while the feedthrough current only occurs at ω_d, thus the motional current is separated from the feedthrough current. The frequency components are shown in figure 4.1.

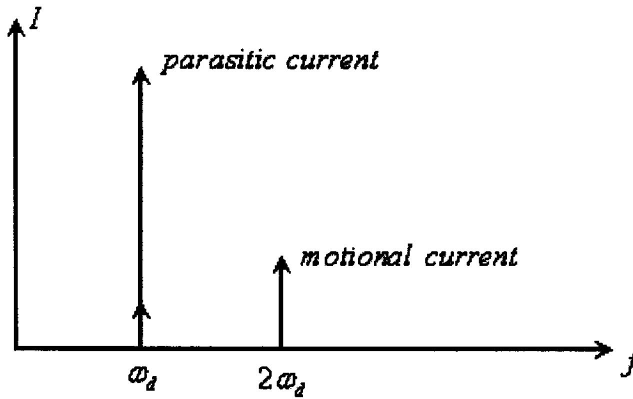

Figure 4.1: The current frequency components

Using the principle of superposition, the steady-state response of the forced oscillation system equation

$$M\frac{d^2x}{dt^2} + c\frac{dx}{dt} + k_x x = F_x(t) \tag{4.4}$$

is given by:

$$x(t) = \frac{\xi}{2k_x}\frac{\partial C}{\partial x}(V_p^{\ 2} + \frac{1}{2}V_d^{\ 2}) + \frac{\xi \frac{\partial C}{\partial x} V_p V_d}{\sqrt{\left(k_x - M\omega_d^{\ 2}\right)^2 + c^2\omega_d^{\ 2}}}\sin(\omega_d t - \varphi_1)$$

$$-\frac{\xi \frac{\partial C}{\partial x} V_d^{\ 2}}{4\sqrt{\left(k_x - 4M\omega_d^{\ 2}\right)^2 + 4c^2\omega_d^{\ 2}}}\cos(2\omega_d t - \varphi_2) \tag{4.5}$$

where

$$\varphi_1 = \arctan(\frac{\omega_d c}{k_x - M\omega_d^{\ 2}}) \tag{4.6}$$

$$\varphi_2 = \arctan(\frac{2\omega_d c}{k_x - 4M\omega_d^{\ 2}}) \tag{4.7}$$

The current at the sense electrode can be expressed as:

$$i_s = i_c + i_m = \xi C \frac{dV_p}{dt} + \xi V_p \frac{dC}{dx}\frac{dx}{dt} = \xi V_p \frac{dC}{dx}\frac{dx}{dt} = i_m \tag{4.8}$$

$$i_s = i_m = \xi^2 V_p (\frac{dC}{dx})^2 V_d \omega_d \left[\frac{V_p}{\sqrt{\left(k_x - M\omega_d^{\ 2}\right)^2 + c^2\omega_d^{\ 2}}}\cos(\omega_d t - \varphi_1) \right.$$

$$\left. + \frac{V_d}{2\sqrt{\left(k_x - 4M\omega_d^{\ 2}\right)^2 + 4c^2\omega_d^{\ 2}}}\sin(2\omega_d t - \varphi_2) \right] \tag{4.9}$$

The current component at ω_d is masked by the feedthrough current, which has the same frequency as the driving signal. However, in the ideal case, the current component at $2\omega_d$ is separated from the feedthrough current.

The current component at $2\omega_d$ is:

$$i_s = i_m = \frac{\xi^2}{2}(\frac{dC}{dx})^2 \frac{V_p V_d^{\ 2}\omega_d}{\sqrt{\left(k_x - 4M\omega_d^{\ 2}\right)^2 + 4c^2\omega_d^{\ 2}}}\sin(2\omega_d t - \varphi_2) \tag{4.10}$$

where dC/dx can be obtained from reference [6] and [7]. If the amplitude of the applied voltages are fixed, thus $\frac{\xi^2}{2}(\frac{dC}{dx})^2 V_p V_d^2$ can be regarded as a constant and is independent of frequency. If we define $Amp(\omega_d)$ as:

$$Amp(\omega_d) = \frac{\omega_d}{\sqrt{\left(k_x - 4M\omega_d^2\right)^2 + 4c^2\omega_d^2}} \tag{4.11}$$

and expressed in decibel, $Amp(\omega_d)$ can fully characterize the system, while the spectrum should shift downward according to $\frac{\xi^2}{2}(\frac{dC}{dx})^2 V_p V_d^2$.

If we consider the system as listed in table 4.1, $Amp(\omega_d)$ in decibel is plotted in figure 4.2.

Table 4.1: The system parameters

Effective mass	$5.4568\times10^{-11}kg$
Damping coefficient	2.2×10^{-7}
Spring constant	$0.58N/m$

According to (2.2), the resonant frequency for the comb drive listed in table 4.1 is:

$$f_0 = \frac{1}{2\pi}\left[\frac{k_x}{M_{eff}}\right]^{\frac{1}{2}} = \frac{1}{2\pi}\left[\frac{0.58}{5.4568\times10^{-11}}\right]^{\frac{1}{2}} = 16408.35Hz \tag{4.12}$$

for the current component at $2\omega_d$, the amplitude reaches maximum at $\frac{1}{2}f_0$, as shown in figure 4.2. The quality factor can be calculated from the –3dB bandwidth as equation (2.7):

$$Q = \frac{f_r}{f_2 - f_1} = \frac{0.5f_0}{f_2 - f_1} \approx \frac{8204.175}{8366.10 - 8046.27} \approx 25 \tag{4.13}$$

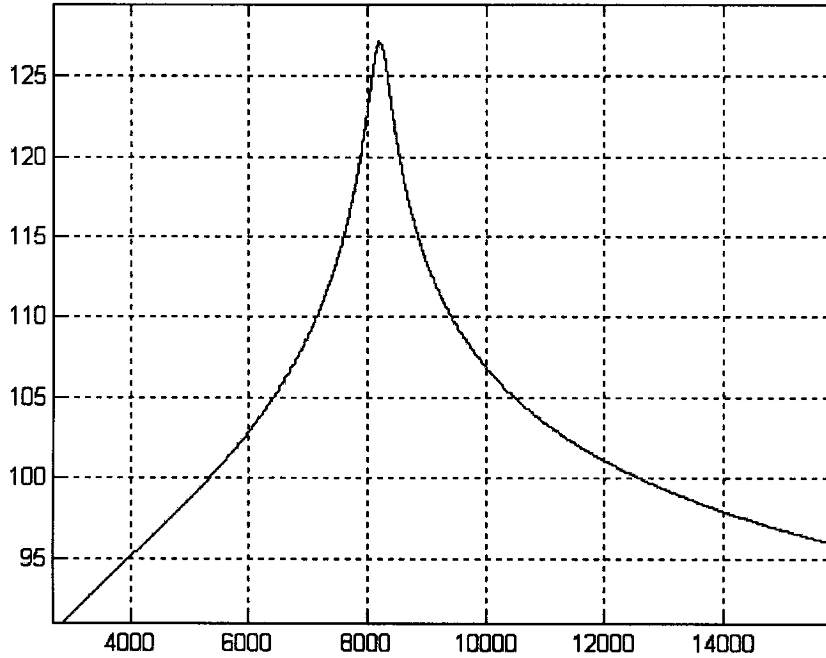

Figure 4.2: The amplitude ($Amp(\omega_d)$) of motional current in logarithm axis

However the harmonic distortion in the output signal of a device makes the frequency doubling measurement very difficult. The harmonic distortion is caused by the presence of frequencies that are not in the input signal. These frequencies are usually a sinusoidal component of a periodic wave or quantity having a frequency that is an integral multiple of the fundamental frequency. The harmonic distortion at $2\omega_d$ will induce feedthrough current, which masks the motional current. Even though the harmonic distortion of the function generator is no greater than –90dB from DC to 50 kHz, the feedthrough current as shown below, makes the measurement very difficult because of the large parasitic capacitance.

$$i_p = C_p \frac{dv}{dt} = C_p \frac{d[v'\sin(2\omega_d t)]}{dt} = 2v'\omega_d C_p \cos(2\omega_d t) \tag{4.14}$$

The only solution left for observing motional current component in frequency domain is mixing measurement, by adding a carrier to the shuttle.

4.2 Mixing Measurement

Figure 4.3.a plots the schematic of mixing frequency measurement at atmosphere. The series LCR equivalent circuit of the comb drive is in parallel with a probe-to-probe parasitic capacitance, as shown in figure 4.3.b. The current spectrum at sense electrode in figure 4.3.c illustrates the motional current at ω_d is amplitude modulated by the carrier to frequencies at $\omega_c - \omega_d$ and $\omega_c + \omega_d$, successfully separated from the parasitic feedthrough. The output is amplified by a transmittance amplifier, then enter into the "Demod" box, where the signal passes a bandpass filter (as shown in Figure 4.3.c) to remove frequency component at ω_d, and then demodulated by a balanced Gilbert cell multiplier. Finally the demodulated spectrum as shown in Figure 4.3.d enters into a low pass filter, generating a signal near ω_0 which is suitable for input to spectrum analyzer.

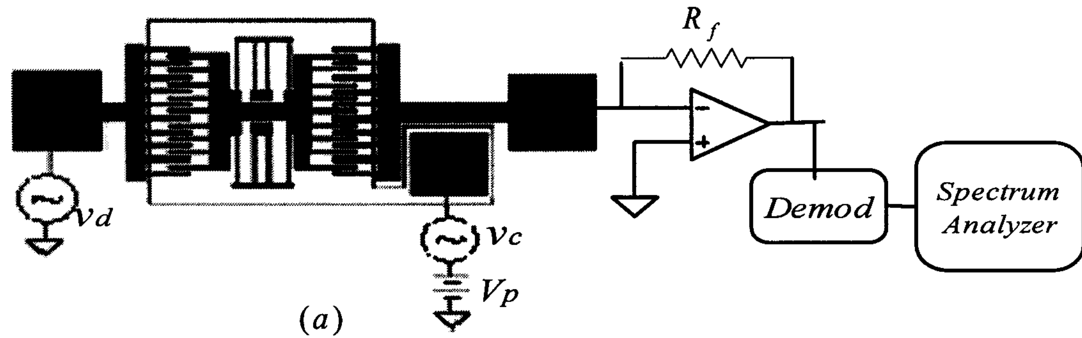

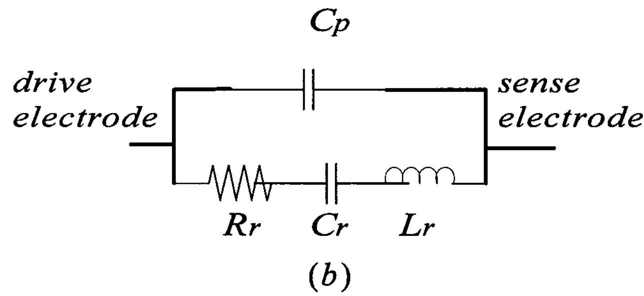

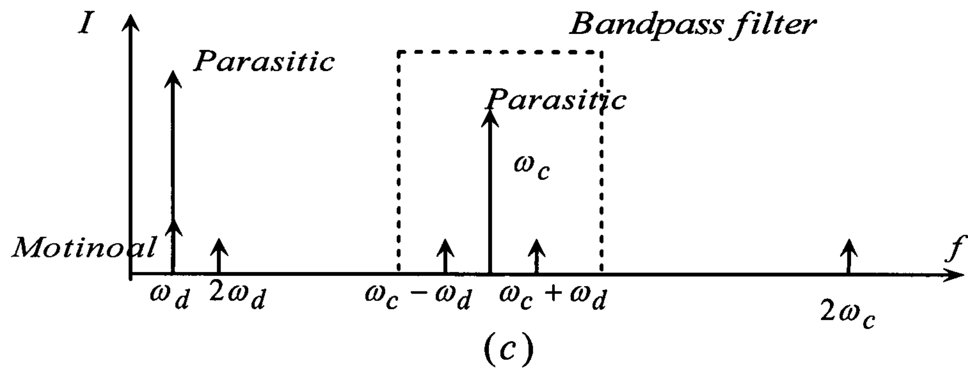

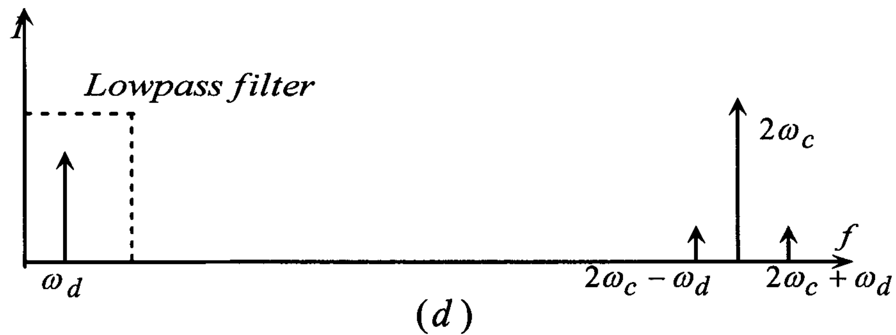

Figure 4.3: a) Schematic of mixing frequency measurement for spectrum analysis; b) equivalent circuit of the resonator shown in a); c) current spectrum at the sensing electrode; d) the spectrum after demodulation

Under the bias configuration of Figure 4.3.a, the electrostatic force, including fringing effect, can be calculated as:

$$F = \frac{\xi}{2}\frac{\partial C}{\partial x}(V_p + V_d \sin\omega_d t + V_c \sin\omega_c t)^2$$

$$= \frac{\xi}{2}\frac{\partial C}{\partial x}\left[V_p^2 + \frac{1}{2}V_d^2 + \frac{1}{2}V_c^2 + 2V_pV_d\sin\omega_d t + 2V_pV_c\sin\omega_c t - \frac{1}{2}V_d^2\cos 2\omega_d t \right.$$

$$\left. -\frac{1}{2}V_c^2\cos 2\omega_c t + V_dV_c\cos(\omega_c t - \omega_d t) - V_dV_c\cos(\omega_c t + \omega_d t) \right] \quad (4.15)$$

The electrostatic force now has frequency components at ω_d, ω_c, $2\omega_d$, $2\omega_c$, $\omega_c - \omega_d$, $\omega_c + \omega_d$ and DC. The resonance can be only excited by the frequency component at ω_d by carefully choosing the carrier frequency. The feedthrough currents only occur at frequency components ω_d and ω_c. Thus all the other frequency components are not affected by the parasitic feedthrough and the motional current and parasitic are successfully separated and can be used to evaluate the behavior of the comb drive. The motional current around ω_d is amplitude modulated by the carrier to $\omega_c - \omega_d$ and $\omega_c + \omega_d$, which is called electromechanical amplitude modulation [42].

Using the principle of superposition, the steady-state solution of $M\frac{d^2x}{dt^2} + c\frac{dx}{dt} + k_x x = F_x(t)$ becomes the sum of solutions below:

$$M\frac{d^2x}{dt^2} + c\frac{dx}{dt} + k_x x = \frac{\xi}{2}\frac{\partial C}{\partial x}\left(V_p^2 + \frac{1}{2}V_d^2 + \frac{1}{2}V_c^2 \right) \quad (4.16)$$

$$M\frac{d^2x}{dt^2} + c\frac{dx}{dt} + k_x x = \xi\frac{\partial C}{\partial x}V_pV_d\sin\omega_d t \quad (4.17)$$

$$M\frac{d^2x}{dt^2}+c\frac{dx}{dt}+k_x x=\xi\frac{\partial C}{\partial x}V_pV_c\sin\omega_c t \tag{4.18}$$

$$M\frac{d^2x}{dt^2}+c\frac{dx}{dt}+k_x x=-\frac{\xi}{4}\frac{\partial C}{\partial x}V_d^{\,2}\cos 2\omega_d t \tag{4.19}$$

$$M\frac{d^2x}{dt^2}+c\frac{dx}{dt}+k_x x=-\frac{\xi}{4}\frac{\partial C}{\partial x}V_c^{\,2}\cos 2\omega_c t \tag{4.20}$$

$$M\frac{d^2x}{dt^2}+c\frac{dx}{dt}+k_x x=\frac{\xi}{2}\frac{\partial C}{\partial x}V_dV_c\cos(\omega_c t-\omega_d t) \tag{4.21}$$

$$M\frac{d^2x}{dt^2}+c\frac{dx}{dt}+k_x x=-\frac{\xi}{2}\frac{\partial C}{\partial x}V_dV_c\cos(\omega_c t+\omega_d t) \tag{4.22}$$

and the steady-state response is:

$$x(t)=\frac{\xi}{2k_x}\frac{\partial C}{\partial x}(V_p^{\,2}+\frac{1}{2}V_d^{\,2}\frac{1}{2}V_c^{\,2})$$

$$+\frac{\xi\frac{\partial C}{\partial x}V_pV_d}{\sqrt{\left(k_x-M\omega_d^{\,2}\right)^2+c^2\omega_d^{\,2}}}\sin(\omega_d t-\phi_1)+\frac{\xi\frac{\partial C}{\partial x}V_pV_c}{\sqrt{\left(k_x-M\omega_c^{\,2}\right)^2+c^2\omega_c^{\,2}}}\sin(\omega_c t-\phi_2)$$

$$-\frac{\xi\frac{\partial C}{\partial x}V_d^{\,2}}{4\sqrt{\left(k_x-4M\omega_d^{\,2}\right)^2+4c^2\omega_d^{\,2}}}\cos(2\omega_d t-\phi_3)-\frac{\xi\frac{\partial C}{\partial x}V_c^{\,2}}{4\sqrt{\left(k_x-4M\omega_c^{\,2}\right)^2+4c^2\omega_c^{\,2}}}\cos(2\omega_c t-\phi_3)$$

$$+\frac{\xi\frac{\partial C}{\partial x}V_cV_d}{2\sqrt{\left(k_x-M(\omega_c-\omega_d)^2\right)^2+c^2(\omega_c-\omega_d)^2}}\cos(\omega_c t-\omega_d t-\phi_5)$$

$$-\frac{\xi\frac{\partial C}{\partial x}V_cV_d}{2\sqrt{\left(k_x-M(\omega_c+\omega_d)^2\right)^2+c^2(\omega_c+\omega_d)^2}}\cos(\omega_c t+\omega_d t-\phi_6) \tag{4.23}$$

where

$$\phi_1=\arctan\left(\frac{\omega_d c}{k_x-M\omega_d^{\,2}}\right), \tag{4.24}$$

$$\phi_2 = \arctan(\frac{\omega_c c}{k_x - M\omega_c^2}), \tag{4.25}$$

$$\phi_3 = \arctan(\frac{2\omega_d c}{k_x - 4M\omega_d^2}), \tag{4.26}$$

$$\phi_4 = \arctan(\frac{2\omega_c c}{k_x - 4M\omega_c^2}), \tag{4.27}$$

$$\phi_5 = \arctan(\frac{c(\omega_c - \omega_d)}{k_x - M(\omega_c - \omega_d)^2}) \tag{4.28}$$

and

$$\phi_6 = \arctan(\frac{c(\omega_c + \omega_d)}{k_x - M(\omega_c + \omega_d)^2}) \tag{4.29}$$

Now we can decide the sensing current at the sense electrode according to (4.2) and parasitic current according to (4.3). The voltage difference between shuttle and the sensing electrode equals to the sum of DC bias and the carrier signal.

If we focus on the current component at $\omega_c - \omega_d$, the motional current can be expressed:

$$i_{m,lsb} = \xi V_s \frac{dC}{dx}\frac{dx}{dt} = \left(\frac{dC}{dx}\right)^2 \frac{\xi^2 V_p V_d V_c}{2} \left(\frac{\omega_d}{\sqrt{\left(k_x - M\omega_d^2\right)^2 + c^2\omega_d^2}} \sin(\omega_c t - \omega_d t + \phi_1) \right.$$

$$\left. - \frac{(\omega_c - \omega_d)}{\sqrt{\left(k_x - M(\omega_c - \omega_d)^2\right)^2 + c^2(\omega_c - \omega_d)^2}} \sin(\omega_c t - \omega_d t - \phi_5) \right) \tag{4.30}$$

where $V_s = V_p + v_c$.

Using the product and sum formulas of the trigonometry to express ϕ_1 and ϕ_5, equation (4.30) can be expressed in the form of:

$$i_{m,lsb} = \left(\frac{dC}{dx}\right)^2 \frac{\xi^2 V_p V_d V_c}{2}\left[A\sin(\omega_c - \omega_d)t + B\cos(\omega_c - \omega_d)t\right]$$

$$= \left(\frac{dC}{dx}\right)^2 \frac{\xi^2 V_p V_d V_c}{2}\sqrt{A^2 + B^2}\, Sin(\omega_c t - \omega_d t + \varphi) \tag{4.31}$$

where

$$\tan\varphi = \frac{B}{A} \tag{4.32}$$

$$A = \frac{\omega_d (k_x - M\omega_d^{\ 2})}{(k_x - M\omega_d^{\ 2})^2 + c^2\omega_d^{\ 2}} - \frac{(\omega_c - \omega_d)(k_x - M(\omega_c - \omega_d)^2)}{(k_x - M(\omega_c - \omega_d)^2)^2 + c^2(\omega_c - \omega_d)^2} \tag{4.33}$$

$$B = \frac{c\omega_d^{\ 2}}{(k_x - M\omega_d^{\ 2})^2 + c^2\omega_d^{\ 2}} + \frac{c(\omega_c - \omega_d)^2}{(k_x - M(\omega_c - \omega_d)^2)^2 + c^2(\omega_c - \omega_d)^2} \tag{4.34}$$

Alternatively, if we define $C = \xi(C_0 + C_m \cos\omega \cdot t)$, where C_0 is the static finger-to-finger overlap capacitance and C_m is the capacitance occurred at the maximum displacement, the lower side band of the motional current in terms of C_m can be expressed as:

$$i_{m,lsb} = \left(v(t)\frac{dC}{dt}\right)_{lsb} = -\frac{1}{2}\xi C_m \omega_d V_c \cos(\omega_c - \omega_d)t \tag{4.35}$$

Comparing equation (4.35) and (4.31), C_m can be expressed in phasor form:

$$C_m = V_p V_d \xi \left({}^{dC}\!/\!_{dx}\right)^2 \frac{\sqrt{A^2 + B^2}}{\omega_d} \angle(\varphi + 90^\circ) \tag{4.36}$$

Solving equation (4.2) at resonance in terms of C_m, the output of the bandpass filter i_0 can be expressed as:

$$\begin{aligned} i_0 &= \xi C_0 \omega_c V_c \cos(\omega_c t) + \frac{\xi}{2} C_m V_c (\omega_c - \omega_d)\cos(\omega_c t - \omega_d t) \\ &+ \frac{\xi}{2} C_m V_c (\omega_c + \omega_d)\cos(\omega_c t + \omega_d t) \end{aligned} \tag{4.37}$$

Demodulation can be achieved by multiplying i_0 by an effective multiplier $R\sin(\omega_c t+\theta)$, where R is determined by the transmittance amplifier and the effective gain of Gilbert cell multiplier [42]. The output of the "Demod" box is:

$$V_o = \frac{1}{2}\xi C_m V_c R \sqrt{(\omega_c \sin\theta)^2 + (\omega_d \cos\theta)^2} \angle \arctan(-\frac{\omega_d \cos\theta}{\omega_c \sin\theta})$$

To maximize the output voltage at resonance, the multiplier should be chosen with $\theta = 90^\circ$, a phase shifter is need for this purpose. Thus V_o becomes:

$$V_o = \frac{1}{2}\xi^2 V_p V_d V_c R \left(dC/dx \right)^2 \frac{\omega_c \sqrt{A^2+B^2}}{\omega_d} \angle(\varphi + 90^\circ)$$

where dC/dx can be obtained from reference [6] and [7]. If the amplitude of the applied voltages and R are fixed, thus $0.5\xi^2 V_p V_d V_c R \cdot (dC/dx)^2$ can be regarded as a constant and is independent of frequency. If spectrum is plotted in decibel, $(\omega_c/\omega_d)(\sqrt{A^2+B^2})dB$ can fully characterize the system, while the spectrum should shift downward according to $0.5\xi^2 V_p V_d V_c R \cdot (\partial C/\partial x)^2 dB$.

Using the system specifications listed in Table 4.2, the plot of $(\omega_c/\omega_d)(\sqrt{A^2+B^2})dB$ is shown figure 4.4. The quality factor may be calculated using the –3dB bandwidth:

$$Q = \frac{f_r}{f_2 - f_1} = \frac{f_0}{f_2 - f_1} \approx \frac{16964}{17283 - 16643} = 26.5$$

which is in the reported range for comb drive operating at air pressure [6],[8].

Figure 4.5 shows the frequency response for systems with different spring constants, $0.62 N/m$, $1.24 N/m$ and $1.86 N/m$ from left to right. As the spring constant

increase, the resonant frequency shifts to higher frequency and the amplitude decreases.

In order to increase the quality factor, the device should operate in vacuum to eliminate loss due to fluidic damping mechanisms. Figure 4.6 compares the spectrum of the system operating in two levels of vacuum with damping coefficients of $1e-7$ and $1.4e-8$ with atmosphere pressure.

TABEL 4.2: The System Parameters

Effective mass	$5.4568 \times 10^{-11} kg$
Spring constant	$0.62 N/m$
Damping coefficient	2.2×10^{-7}
Carrier frequency	100kHz

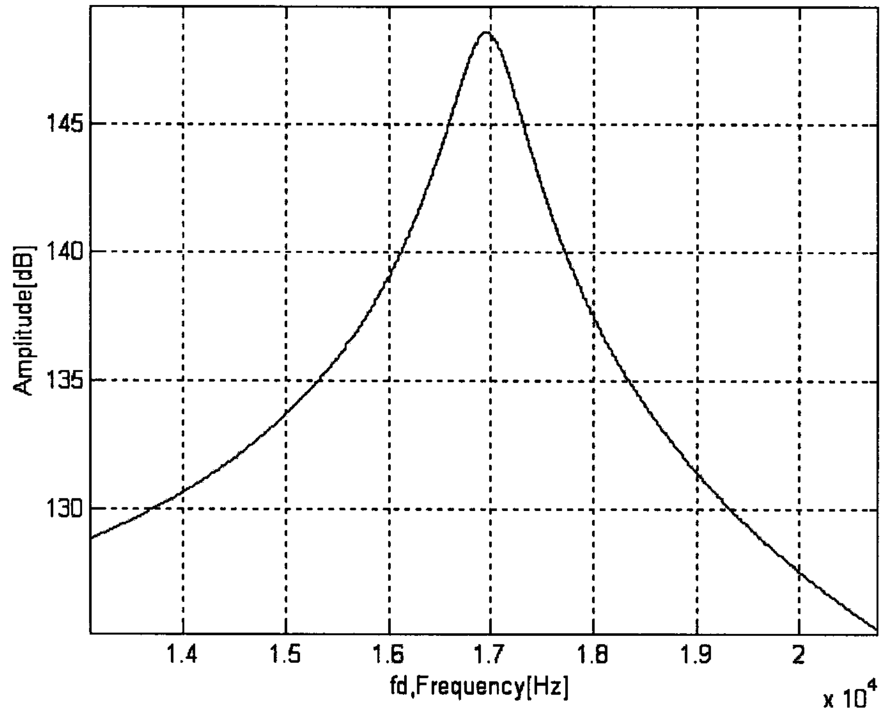

Figure 4.4: Plot of frequency response at atmosphere

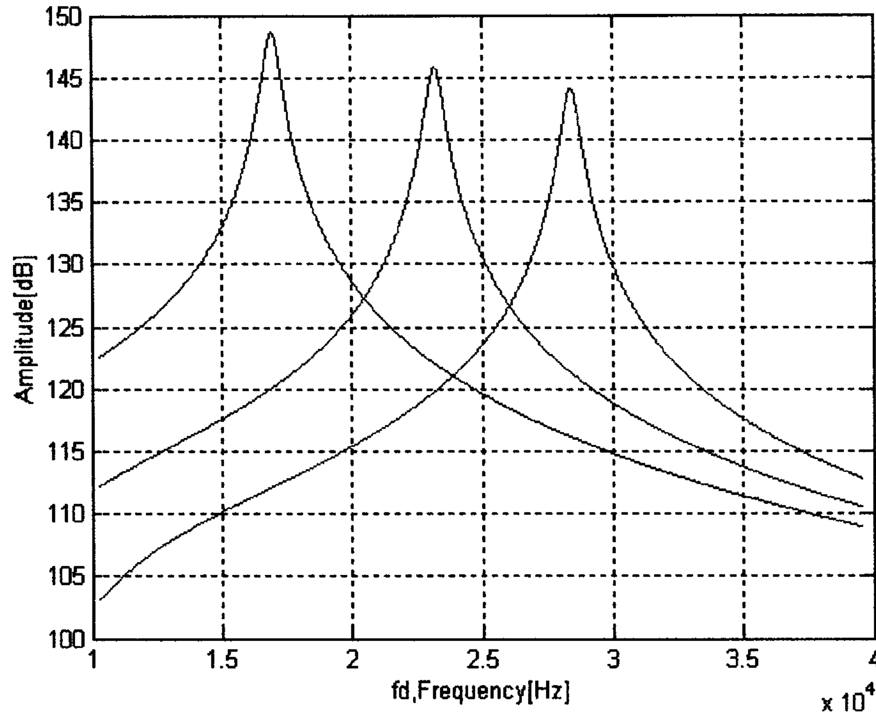

Figure 4.5: Comparison of spectrum with different spring constants at atmosphere

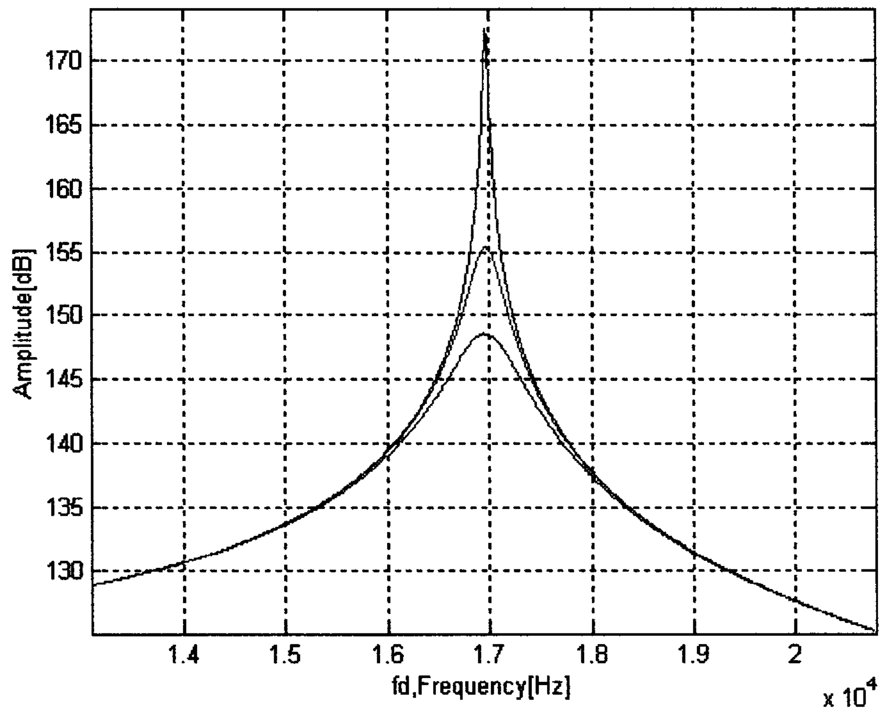

Figure 4.6: Comparison of spectrum operating at different levels of pressures

At pressures in the range of 0.1-1 mtorr, viscous gas damping ceases to be the dominant energy-dissipation mechanism and the intrinsic material damping mechanisms become dominant. And the quality factor is maximized and in the range of 50 000 to 500 000 [43].

CHAPTER 5 Experiment Result

This chapter presents the result of the experiments. After verification of the success of HF release and critical point drying in carbon dioxide, and complement of dual in line bonding which enables the measurement in the vacuum chamber of SEM, the devices are ready for measurement. Time domain observation and measurements are performed in the probe station and SEM, while the frequency domain measurements are carried out at atmosphere pressure and at vacuum pressure. Due to the difficulty of probing and bonding caused by the lubricants, only those devices without lubrication are taken under experiment. Verification of successful release and stimulation with high DC voltage, which is used to minimize the stiction, are carried out each time before experiment. By using a spectrum analyzer, the frequency spectrum of several devices is measured. The measurement in the vacuum is more reliable because of absence of air damping and noise due to the instability of the probe station and unshielded wires.

5.1 Experimental Instruments:

5.1.1 Micro Manipulation Probe Station

The probe station Micro Manipulation's Model 6000 Integrated Circuit Inspection Station is used for preliminary measurement. The station is composed of a microscope system and three 3-D micromanipulators. Connection to the macro world is through the probing of the micromanipulators. The die can be fixed in the station by the vacuum subsystem. The micromanipulator can also be used to mechanically stimulate the device. The probe station is very easy to use and provides great flexibility, and it is used for verification of release, application of large DC signal for stimulation, and preliminary measurement. However due to its susceptibility of

external vibration and noise of the unshielded wire, more sophisticated instruments should be used to obtain accurate results.

5.1.2 HITACHI S-520 Scanning Electron Microscope

The scanning electron microscope (SEM) is a microscope that uses electrons rather than light to form an image. The electron source in side the SEM generates a beam of electrons in a vacuum. That beam is collimated by electromagnetic condense lenses, focused by an objective lens, and scanned across the surface of the sample by electromagnetic deflection coils. The primary imaging method is by collecting secondary electrons that are released by the sample. The secondary electrons are detected by a scintillation material that produces flashes of light from the electrons. The light flashes are then detected and amplified by a photomultiplier tube. By correlating the sample scan position with the resulting signal, an image can be formed that is strikingly similar to what would be seen through an optical microscope.

The advantages of SEM include:

- Large depth of field, which allows a large amount of sample to be in focus at one time.
- High resolution, which means that closely spaced features can be examined at a high magnification.
- Preparation of the sample is relatively easy since most SEMs only require the sample to be conductive.

The HITACHI S-520 Scanning Electron Microscope and its block diagram are presented in Figure 5.1.

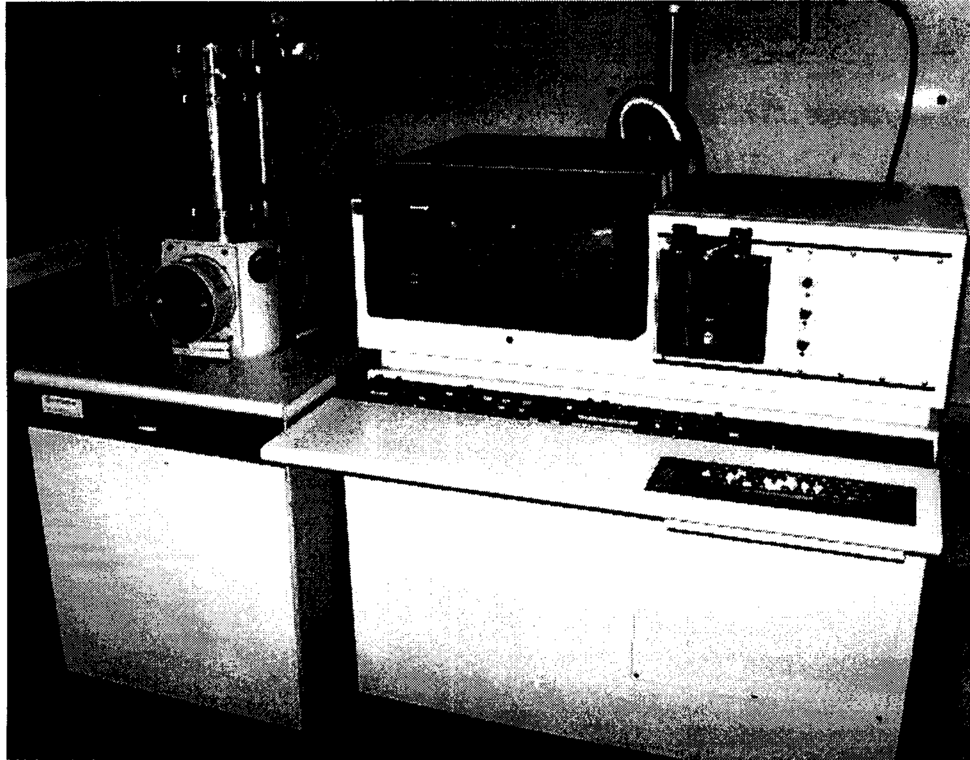

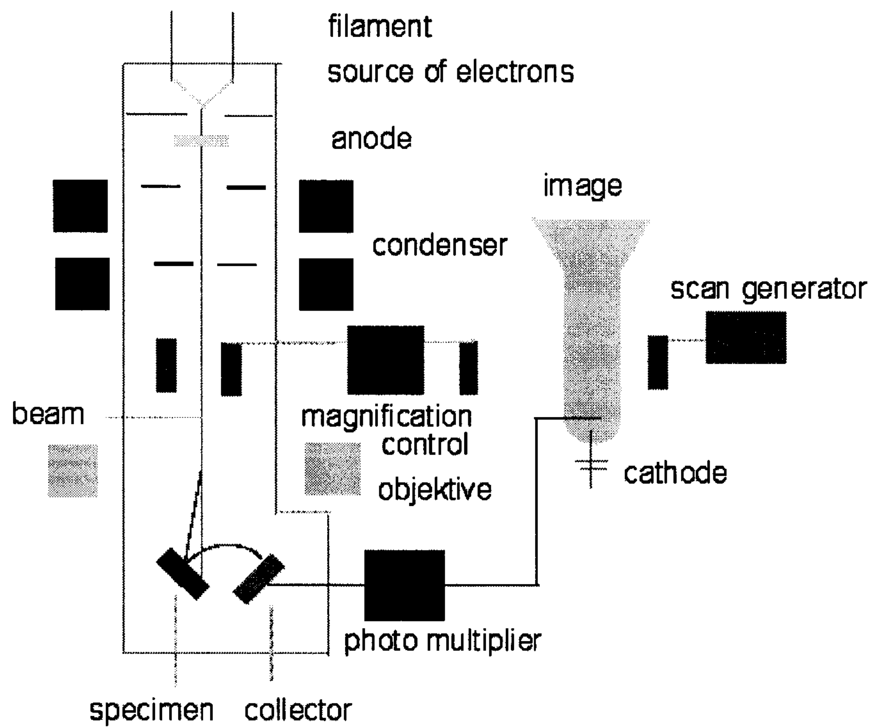

Figure 5.1: HITACHI S-520 Scanning Electron Microscope and its block diagram

5.1.3 SR770 FFT Spectrum Analyzer (DC – 100 kHz)

The SR770 spectrum analyzer is on loan for short term from CMC's equipment pool, and shared with Mcgill University. The SR770 FFT Spectrum Analyzer uses a particular algorithm, called the Fast Fourier Transform (FFT), for computing the DFT. The discrete version of the Fourier transform is called the Discrete Fourier Transform. This transform takes digitized time domain data and computes the frequency domain representation. While normal Fourier theory is useful for understanding how the time and frequency domain relate, the DFT allows us to compute the frequency domain representation of real-world time domain signals. This brings the power of Fourier theory out of the world of mathematical analysis and into practical measurements. The FFT and DFT produce the same result and the feature is commonly referred to as simply the FFT. Figure 5.2 shows a sampled time domain waveform and the resulting frequency domain plot using the FFT.

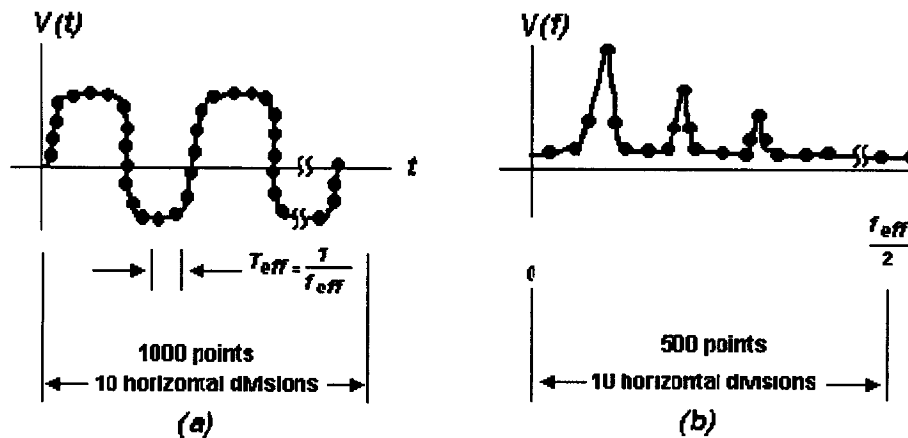

Figure 5.2: a) sampled time domain waveform and the resulting frequency domain plot using Fast Fourier Transform

The SR770 is a single-channel, 100 kHz FFT spectrum analyzer with a real-time bandwidth of 100 kHz. The SR770 additionally includes a low-distortion, synthesized source allowing you to measure the transfer functions of the electronic and mechanical systems. Figure 5.3 presents the SR770 FFT spectrum analyzer, and

table 5.1 lists the main parameters of the instrument.

Figure 5.3: SR770 FFT Spectrum Analyzer

Table 5.1: The main parameters of SR770 FFT Spectrum Analyzer

Source amplitude range	0.1 mV_p to 1.0 V_p
Source Frequency range	Dc to 100 kHz
Input Impedance	1 Mohm, 15 pF
Dynamic range	90 dB

5.1.4 Tektronix 2710 Spectrum Analyzer (1MHz – 1.2GHz)

The front panel of the 2710 is divided into nine major groupings: frequency control and markers, frequency span/division, resolution bandwidth, reference level, vertical scaling, display and storage, sweep and triggering, utilities, and miscellaneous controls.15 minute warm up is required for the analyzer to reach its listed operating specification. The procedure includes restoring factory default settings, calibration and measurement, calculation if necessary. Then central frequency, reference level, frequency span/div should be adjusted for optimal readout. This equipment is available in ECE department, Concordia University.

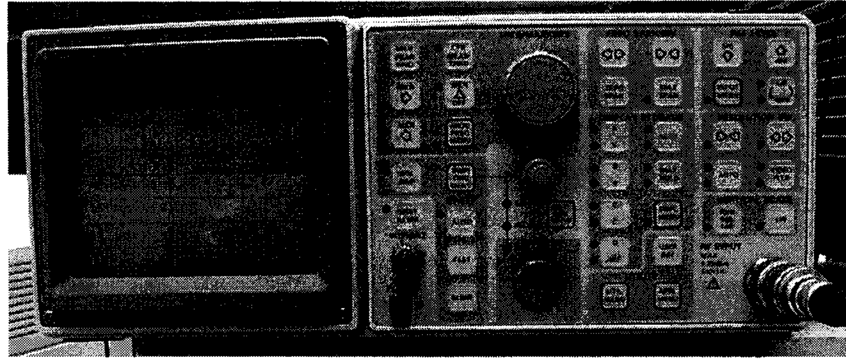

Figure 5.4: Tektronix 2710 Spectrum Analyzer

5.2 Time Domain Experimental Data

5.2.1 Probe Station Observations

Figure 3.2 – 3.4 present the pictures taken through the microscope of the probe station, showing the devices after HF release and post-processing. In this part the device is connected with AC and DC signals through microprobes and observation of vibration are reported.

According to the equation 4.1, there is a static force proportional to DC voltage V_p^2, which helps to stimulate the comb drive, a DC voltage of 50V is applied to the shielding and movable structure. Considering the large damping coefficient at atmosphere, the structure is driven at two ports by AC signals that have 180° phase difference.

In this thesis, operational amplifier LM741 is used to build an inverter. The connection diagram of LM741 and inverter circuit configuration is shown in Figure 5.5, where A_{ol} is the open loop gain and B is the bandwidth. The product of the open loop gain and the bandwidth is typically in the range of 10^5-10^6, and its reciprocal can be neglected. Thus as long as R_f equals to R_s, the output of the LM741 has the same amplitude but 180° phase difference with the input signal. A DC voltage of 22V is

supplied to pin7 and –22V is supplied to pin4. Two resistors of 10 kΩ are used as the R_f and R_s. The inverter works well under 20kHz with input 16V peak-to-peak, but the amplitude of output signal degenerates at higher frequency. The input and output signal are examined in an oscilloscope with two channels before connected to the device.

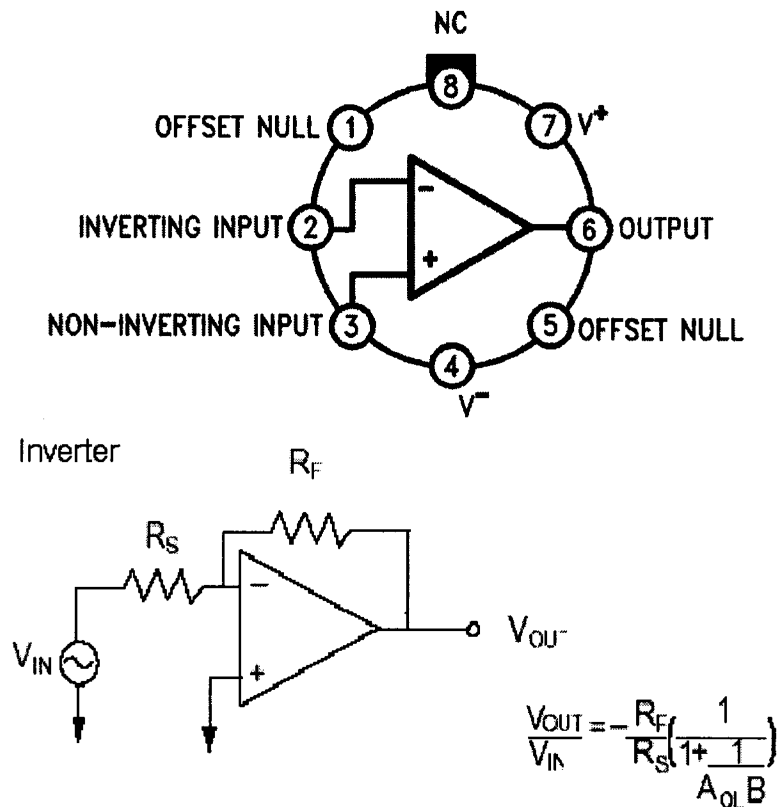

Figure 5.5: a) the connection diagram of LM741; b) the circuit configuration of inverter

The circuit schematic is shown in Figure 5.6. Before voltage is applied, stimulation with a microprobe is performed to minimize the large stiction due to long rest time. The probes connected to the two fixed fingers are supplied with AC signals with same amplitude, 180°-phase difference. The signal is 16 volts peak to peak and with frequency sweeping upward from 1 kHz. A DC voltage of 50 volts is connected to the movable fingers through anchors and dimples.

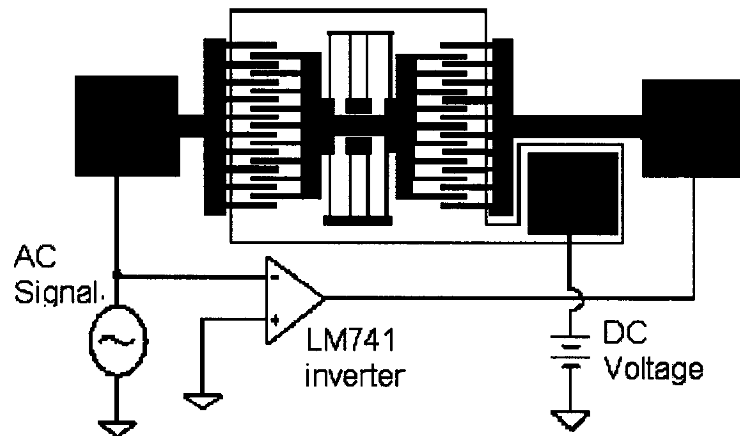

Figure 5.6: Circuit schematic indicating the electrical connections necessary for driving a lateral resonant microstructure into resonance in probe station

Due to the air damping and noise mentioned before, measurement is not accurate and it is very hard to observe the maximum deflection. Figure 5.7 presents the observation on a device in category 4 (balanced comb drive with an attached cantilever beam). Figure 5.7 a) shows four vibrating spring beam when the frequency is at 17 kHz, which is near the predicted resonant frequency; b) is the layout of the scale used to measure the displacement and c) shows the blur envelope of the cantilever beam tip, from which the displacement can be determined to be around 2 μm. The unbalanced comb drive with a cantilever has the similar observation, however for devices in category 3 and 5 (with engaged microengine), no vibration is observed.

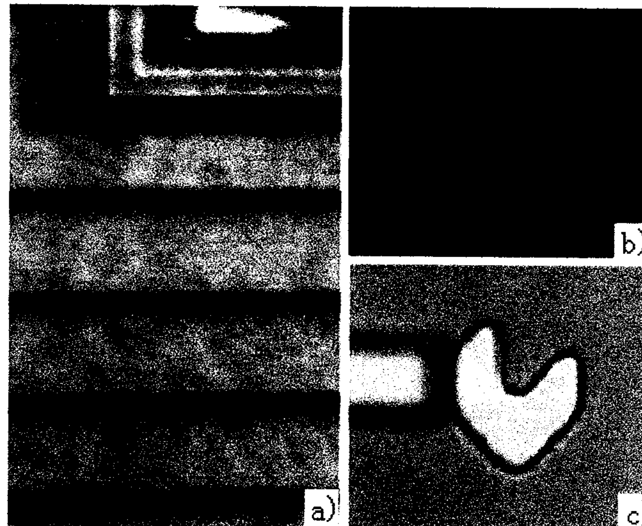

Figure 5.7: The probe observation of the vibration; a) the spring blur, b) the layout of the scale, c) the blur of the cantilever beam tip

5.2.2 SEM Observations

Direct observation in SEM (scanning electron micrograph) is carried out first to find out the resonant frequency and resonant mode. The SEM acceleration voltage is limited to minimize charging from the scanning electron beams. Figure 5.8.a presents one unbalanced comb drive (in category 1) with a beam attached on the right to transfer the linear lateral motion to rotational motion through rack and pinion engagement. The initial rotation of the pinion is due to fluid force in HF release process and it indicates that the device is successful released; Figure 5.8.b shows a balanced comb drive with attached cantilever beams at both sides (category 4).

In Figure 5.9, the sample is rotated 60 degree from horizontal. It is obvious that the movable fingers are lower than the fixed fingers. This phenomenon is due to the adhesion force of remaining charge after post-processing. It can be calculated that the sink is around 200nm.

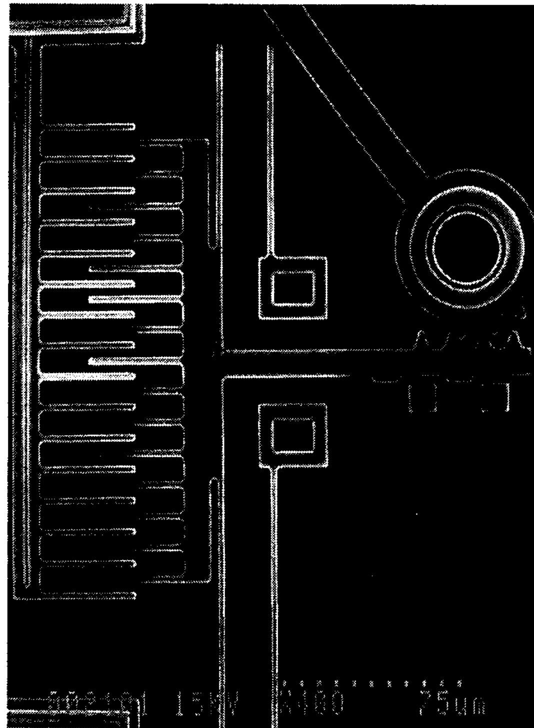

(a)

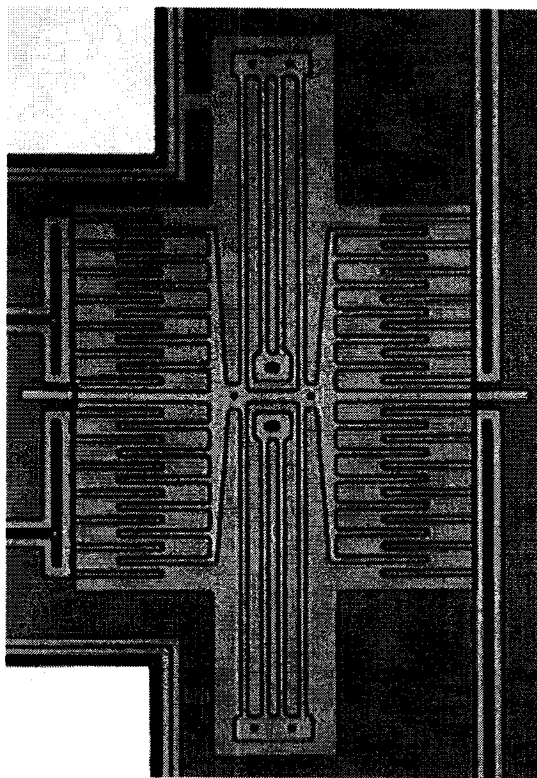

(b)

Figure 5.8: Unbalanced (a) comb drive for testing and balanced (b) comb drive as power source

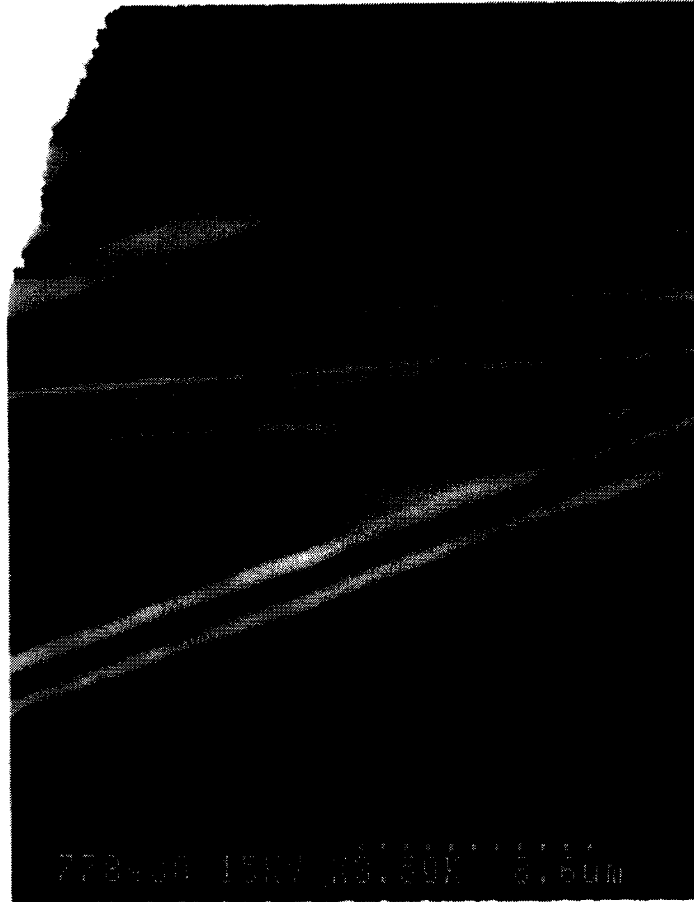

Figure 5.9: SEM observation of sink of movable fingers when no voltage is applied

The below measurement is carried out in SEM vacuum chamber, which has a pressure around 10^{-5} Torr. The low pressure almost eliminates the losses due to fluidic damping mechanisms. The lateral electrostatic force required to sustain the resonance is reduced by the quality factor Q, which is around 50 000, where at atmosphere pressure, $Q<100$ [36]. The intrinsic material damping mechanisms become dominant [44].

In each SEM section, only one device can be measured. The angle of tile is fixed for comparison between different structures. The lateral displacement is evaluated by accurately measuring the SEM images with a set of standard line widths.

The electrical signal is supplied into the vacuum chamber through a BNC connecter in the SEM. Inside the vacuum chamber, two small wires are soldered to the BNC connecter and the other ends are connected to the proper pins in the package of the device. Because the shielding of the BNC cable is connected to ground, there is only one electrical signal is supplied into the chamber and we need to change the circuit schematic other than that in Figure 5.6. The circuit schematic used for measurement in SEM chamber is shown in Figure 5.10. The movable fingers and the shielding are connected to ground and there is no vertical levitation problem which is caused by charge repellence. In the other hand, the sink problem indicated in Figure.5.9 may be reduced by the charging from the incoming electron beam.

In Figure 5.10, Agilent function generator capable of up to 100 kHz with a resolution of 0.1 Hz is used. The series signal is fed to the device under test through a series resistor to prevent short circuit. At first, the DC voltage of 40 volts and an AC signal of 10 volts peak-to-peak are applied to initiate the vibration. Then the frequency of the function generator is sweeping upward. The resonance is determined when the displacement amplitude reaches maximum. Because in the absence of air damping, the DC and AC signals required to sustain the high-Q resonance can be as low as 5V and 0.1V. After the device has run into vibration, the signals are reduced to prevent nonlinear effects due to large drive voltage.

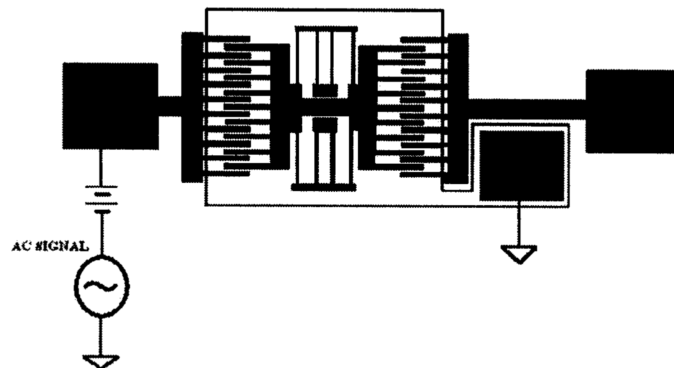

Figure 5.10: Circuit schematic indicating the electrical connections necessary for driving a lateral resonant microstructure into resonance in SEM

Table 5.2 lists the parameters of two typical balanced and unbalanced comb drive used for SEM observation, in which the effective mass is calculated under the assumption that there is no offset and sidewall angle of polysilicon devices fabricated by the Multi-User MEMS Processes. The resonant frequency without the effect of process offset is calculated by equation (2.2), choosing 160Gps as Young's modulus. The resonant frequency including the effects of a distributed mass, residual stress, and compliant support could be developed by the analytical model proposed in [18].

Table 5.2: Balanced and unbalanced Comb Drive Parameters

Parameter	Balanced comb	Unbalanced comb
Folded-Beam Length	200 μm	200 μm
Folded-Beam Width	2 μm	2 μm
Structural Layer Thickness	2 μm	2 μm
Number of Fingers	12 (both sides)	14 (left), 12 (right)
Finger Length	40 μm	40 μm
Finger Width	3 μm	3 μm
Finger Gap Spacing	3 μm	3 μm
Finger engagement	20 μm	20 μm
Width of Cantilever Beam	15 μm	15 μm
Length of Cantilever Beam	80 μm (both sides)	80 μm (right)
Young's Modulus [34]	160-180Gpa	160-180Gpa
Effective Mass	$5.831\times10^{-11}kg$	$5.457\times10^{-11}kg$
System Spring Constant	$0.62N/m$	$0.62N/m$
Predicted Resonant Frequency	16407 Hz	16964 Hz

In the SEM observation, the device engaged with microengine can not be driven into vibration due to the high friction. The balanced comb drive (category 4) presents perfect lateral vibration, while the unblanced comb drives present significant

erratic vibration. Figure 5.11 presents the predicted and measured resonant frequency for 3 balanced comb drives (category 4). The measured resonant frequencies are around 600 Hz higher than the predicted, and this is may caused by process offset, stress residue and higher Yong's Modulus other than 160Gps. However, due to the poor layout and high device density, only several devices could be bonded to the package and measured in SEM.

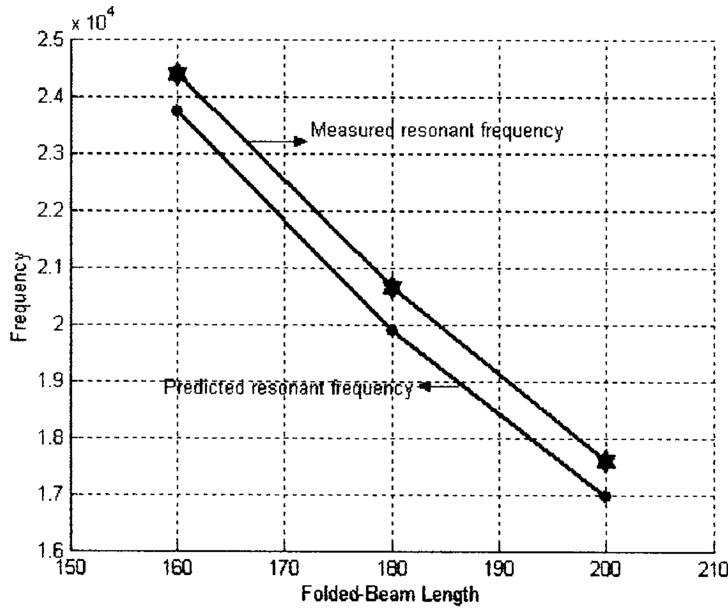

Figure 5.11: Predicted resonant frequency (blue) and the measured resonant frequency (red) for balanced comb drive

The quality factors Q of these three devices are measured using the equation (2.7). f_1 and f_2 are the frequency where the vibration amplitude is around 70% of the maximum displacement. The quality factor plot is shown in Table 5.3.

Table 5.3: Measured quality factor in SEM

Folded-Beam Length	Quality Factor
160 μm	47000±2500
180 μm	44000±2200
200 μm	41500±2000

Figure 5.12.a is the erratic SEM observation of the unbalanced comb drive at resonance. The device and process parameters are listed in table 5.2. The lower set of fingers is fixed and the upper set of fingers is movable. The lateral displacement of the resonator is approximately 3.5 μm, which is calculated with the standard line width. The wave propagation along the upper fingers indicates the vertical vibration and rotation due to asymmetry. The direction of the rotation axis is along the length of folded-beams, as predicted in Figure 2.9. Figure 5.12.b is the picture of the folded-beam at resonant frequency, which indicates the rotation too. Figure 5.12.c is taken at around half resonant frequency and the wave propagation speed along the fingers are around half of that in figure 5.12.a.

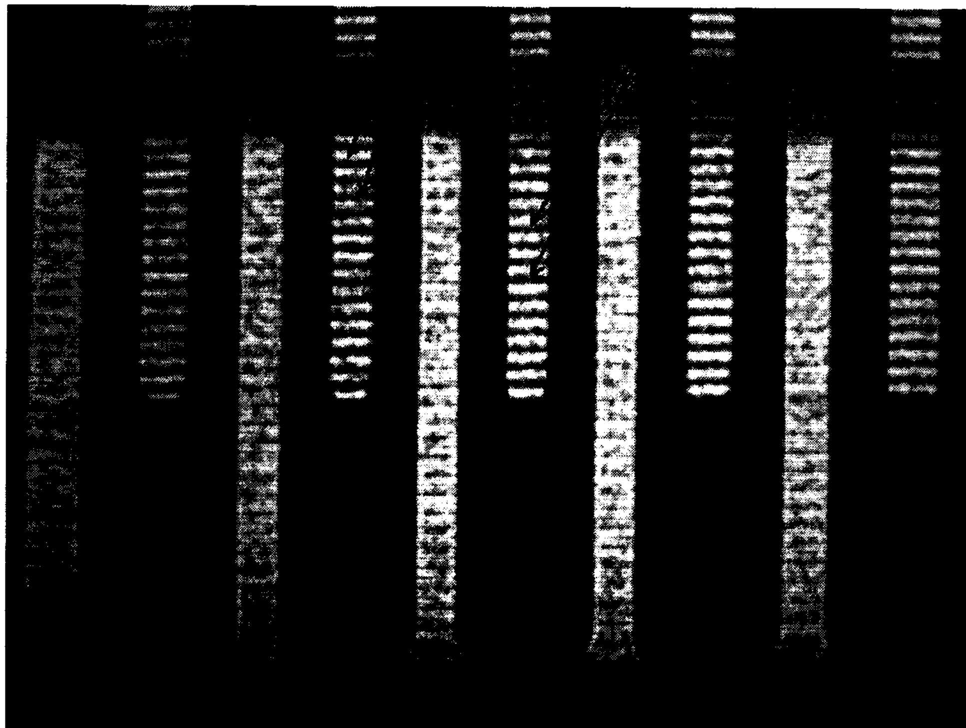

a)

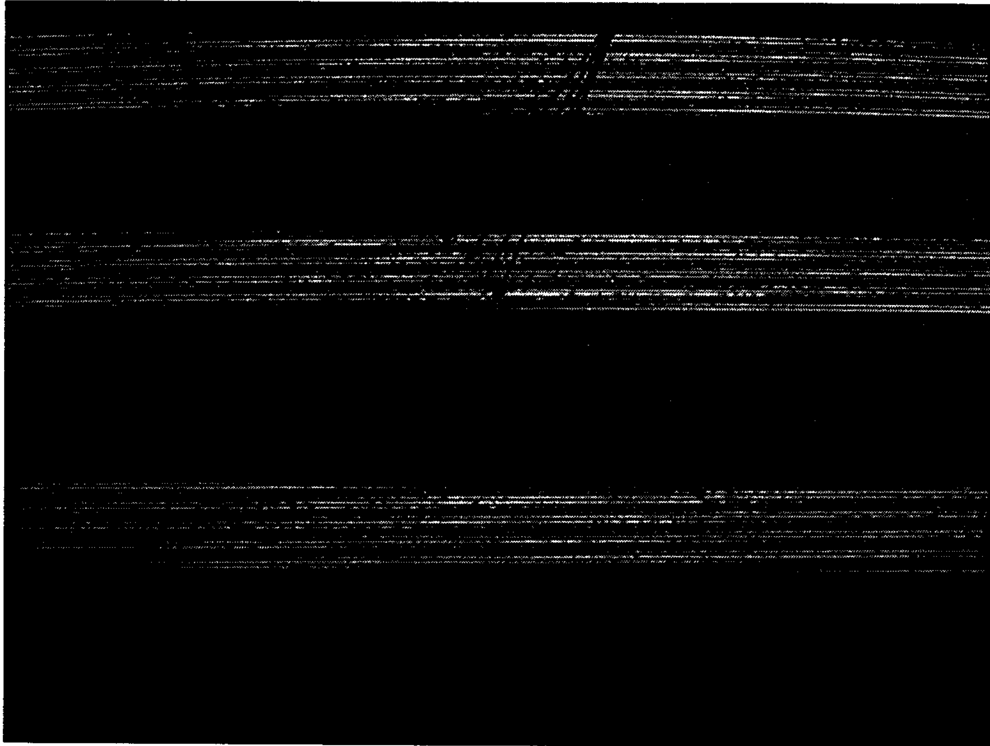

b)

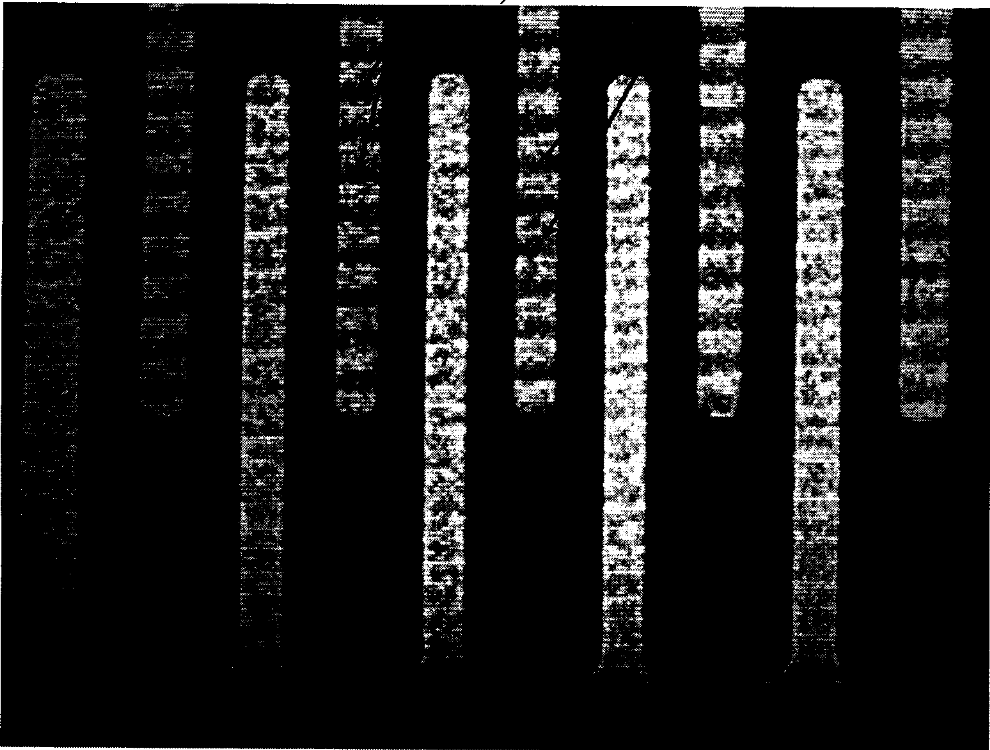

c)

Figure 5.12: SEM observation of comb drive under test. a) wave propagation along the fingers at resonant frequency; b) wave propagation along the folded beam at resonant frequency and c) wave propagation along the fingers at half resonant frequency

In comparison, the resonant mode of balanced comb drive is shown in figure 5.13. It shows that the resonant mode is pure linear, and the displacement is 3.7 μm.

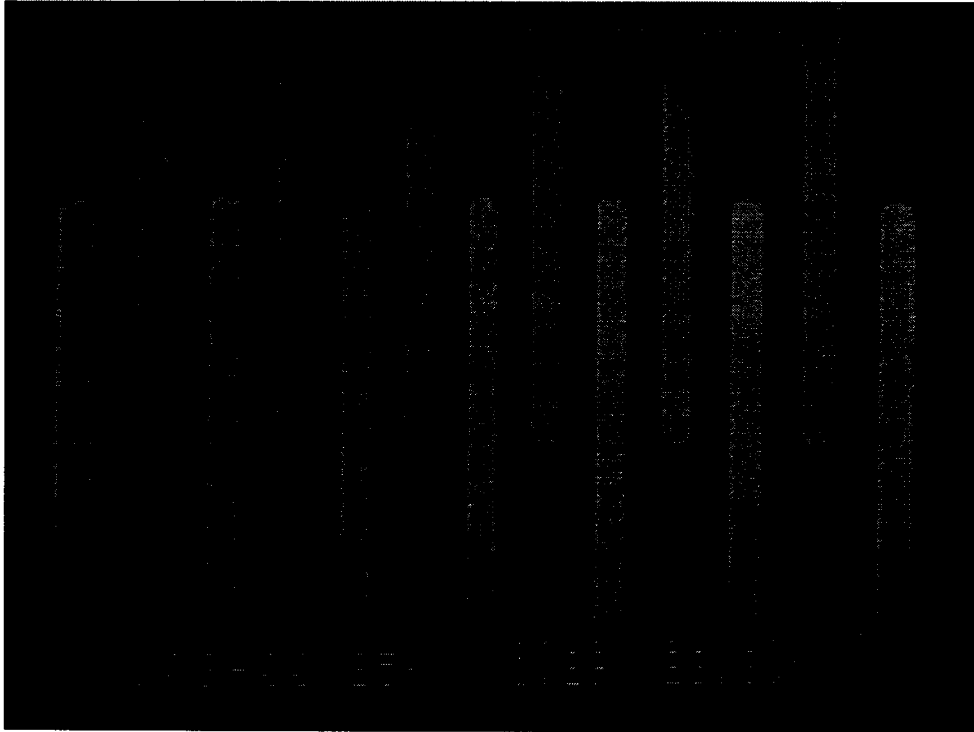

Figure 5.13: The resonant mode of balanced comb drive

5.3 Frequency Domain Data

The same bonded devices are used for mixing frequency measurement at atmosphere. The circuit schematic is shown in figure 5.14. The signal v_d is applied to one fixed electrode. The carrier v_c with higher frequency is connected with DC voltage in series and applied to the shielding and resonator. The sensing output at the other fixed electrode is amplified with an amplifier built with LM741. The complete schematic for the circuit within the "Demod" box is described in [42]. In this case, MC1496 balanced modulator/demodulator is used to build the "Demod" box. Then the output of the "Demod" box is connected to the input of the spectrum analyzer.

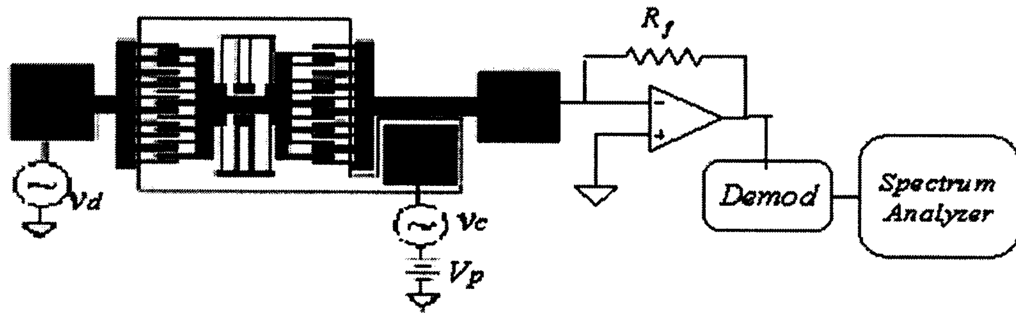

Figure 5.14: Circuit schematic used for mixing frequency measurement

For balanced comb drive, whose parameters are listed in table 5.2, the spectrum measured with mixing frequency method is shown in figure 5.15. The SR770 FFT Spectrum Analyzer (DC – 100 kHz) is used here because it provides better resolution. From figure 5.15, the quality factor calculated using the -3dB bandwidth is around 29. The resonant frequency is around 17620Hz, which is a little bit larger than the predicted value listed in table 5.2, indicating a higher Young's Modulus should be chosen. The measured resonant frequency using mixing frequency method is very close to the one measured in SEM experiment. The spectrum exhibits excellent frequency stability and have the potential for achieving high accuracy in high-speed optical switch. The quality factor at atmosphere versus folded-beam length is shown in figure 5.15. Three different comb drives with different folded-beam length are tested and the quality factor plot is shown in figure 5.16.

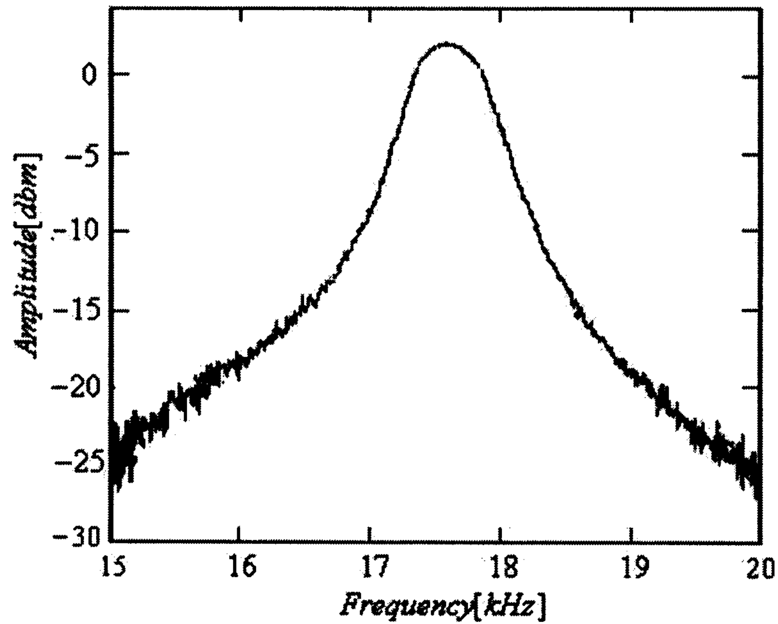

Figure 5.15: Output spectrum for balanced comb drive measured at air pressure

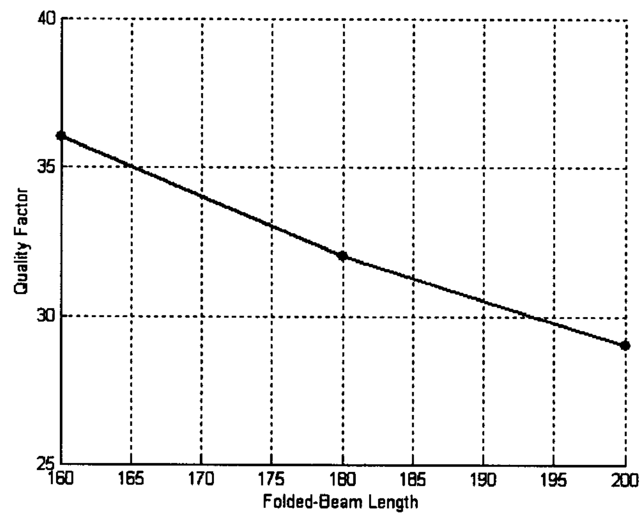

Figure 5.16: Plot of quality factor at atmosphere versus folded-beam length

The frequency spectrum for unbalanced comb drive is shown in figure 5.17. The device parameters are listed in table 5.2. The measurement is carried out with Tektronix 2710 Spectrum Analyzer. The erratic side bands are associated with the rotation frequency components and the impact between movable structure and shielding. The spectrum indicates a loss of stability and system failure may results at those sidebands. The range of instability varies for different resonators and voltage

applied, nevertheless, for unbalanced comb drive tested, erratic behaviour could be induced in at some value or range of frequency.

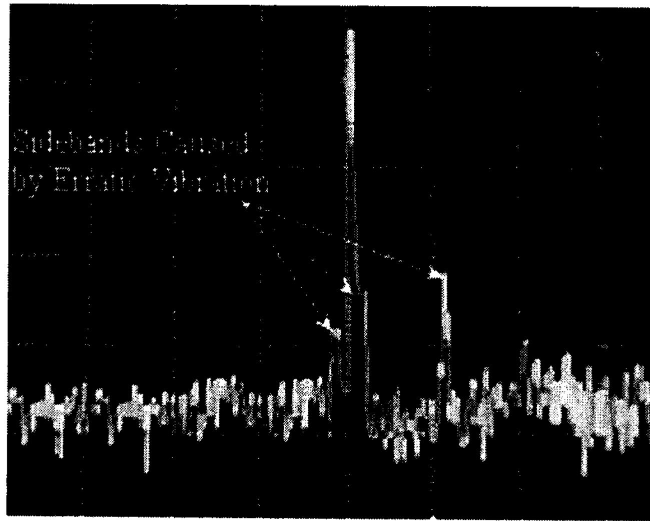

Figure 5.17: Output spectrum for unbalanced comb drive, measured at air pressure. (Y-axis:5dB/div and X-axis:5kHz/div)

CHAPTER 6 Conclusion and Future Work

In this thesis, we have discussed several issues of balanced and unbalanced comb drives including resonant modes, mechanism of lateral displacement and vertical levitation, and the fringing effect, which helps to actuate the comb drive. FEM simulations of the resonance, potential distribution and electrical field distribution are used to study the feasibility of the device. Theoretical formula governing the spectrum are derived. Unbalanced and balanced comb drives are tested in the same configuration. The unbalanced comb drive presents instability in both SEM observations and spectrum analysis, while balanced comb drive eliminates rotational motion and greatly improves the stability.

We have met difficulties in many ways, one is the lubricant, which is used to reduce the stiction, makes the bonding difficult. Another is that comb drive can not initiate the microengine due to stiction.

The goal for the next stage of investigation is to design more sophisticated comb drives used as power source. This could be carried out from several points of view: 1) increase the number of fingers; 2) use double stack structures; 3) multi-comb-drive system to increase drive power; 3) use new fabrication technology other than MUMPs with thicker structure layer; 4) design a mechanism in order to do experiments in the SEM vacuum chamber.

Another focus for future work is vibration spectrum analysis. Though the spectrum at atmosphere is known, the device behavior in vacuum is more interesting. Special vibration spectrum analysis technique should be applied to investigate the device behavior and failure.

REFERENCE

[1] Long-Sheneg Fan, Yu-Chong Tai, and Muller,R.S, "IC-processed electrostatic micro-motors", Electron Devices Meeting, Technical Digest, pp:666-669,1988

[2] Tai,Y.-C, Fan,L-S, Muller,R.S, "IC-processed micromotors: design, technology, and testing", Micro Electro Mechanical Systems, 1989, Proceedings, 'An Investigation of Micro Structures, Sensors, Actuators, Machines and Robots'. IEEE, pp1 – 6, 1989

[3] Ernest J. Garcia, Jeffry J. Sniegowski, "Surface Micromachined microengine", Sensors and Actuators A, vol 48, pp203-214, 1995

[4] Rob Legtenberg, Erwin Berenschot, Miko Elwenspoek, and Jan H. Fluitman, "A Fabrication Process for Electrostatic Microactuators with Integrated Gear Linkages", Journal of Microelectromechanical Systems, Vol.6, No.3, Sep, 1997

[5] W.-H. Juan and S.W.Pang, "High-Aspect-Ratio Si Vertical Micromirror Arrays for Optical Switching", Journal of Microelectromechanical Systems, Vol. 7, No. 2, June 1998.

[6] W.C.Tang, Electrostatic comb drive for resonant sensor and actuator applications; Ph.D dissertation, Univ. California Berkeley, Berkeley, CA, 1990.

[7] William C.Tang, Martin, G.Lim and Roger T. Howe; "ELECTROSTATICALLY BALANCED COMB DRIVE FOR CONTROLLED LEVITATION", Tech. Digest, IEEE Solid-State Sensor and Actuator Workshop, pp23-27, June 1990

[8] W.C.Tang, T.-C.H.Nguyen, and R.T.Howe, "Laterally driven polysilicon resonant microstructures", Sensors and Actuators, vol 20, pp25-32, 1989

[9] P.F.Van Kessel; L.J.Hornbeck; R.E.Meier; M.R.Douglass; "A MEMS-Based Projection Display"; Proceedings of the IEEE, vol.86, no.8, pp1687-1704, August 1998

[10] K.Sato; M.Shikida; "Electrosatic Film Actuator with a Large Vertical Displacement"; Micro Electro Mechanical systems (MEMS'92), Travemunde Germany, pp1-5, 1992

[11] T.Furuhata; T.Hirano; L.H.Lane; R.E.Fontana; L.S.Fan; H.Fujita; "Outer Rotor Surface-micromachined Wobble Micromotor"; IEEE Microelectro Mechanical Systems (MEMS'98), Salt Lake City, pp1-6,1989

[12] G.Cardot; J.Gobet; M.Bogdanski; F.Rudolf; "Fabrication of a Magnetic Transducer Composed of a High-Density Array of Microelectromagnets with On-chip Electronics", Sensors and Actuators A, vol. A43, pp.11-16, 1994

[13] C.H.Ahn; Y.J.Kim; M.G.Allen, "A Fully Integrated Micromachined Toroidal Inductor with a Nickel-Iron core (The Switched DC/DC Boost Converter

Application)"; in 7th International conference on Solid-State Sensor and Actuators, pp.70-73, 1993

[14] Marc.J.Madou; Fundamentals of Microfabrication, The Science of Miniaturization, Second Edition, 2002

[15] M.J.Zdeblick, R.Anderson, J.Janskowski, B.Kline-Schoder, L.Christel, R.Miles and W.Weber, "thermopneumatically Actuated Microvalves and Integrated Electro-fluidic Circuits", Technical Digest, 1994 Solid-State Sensor and Actuator Workshop, pp 251-255, 1994

[16] Claude Deslouis; "Microscopic aspects of surfactants action on flow induced corrosion"; Electrochimica Acta, Vol 48, Issues 20-22, pp.3279-3288, 2003

[17] Toshiki Hirano; Tomotake Furuhata.et.al "Design, Fabrication, and Operation of Submicron Gap Comb-Drive Microactuators"; Journal of Microelectromechanical Systems. Vol.1, No.1, March 1992

[18] Raj K. Gupta; "Electronically Probed Measurements of MEMS Geometries"; Journal of Microelectromechanical Systems, vol.9, No3, Sep, 2000

[19] S.L.Miller, et.al; "Failure modes in surface Micromachined microelectromechanical actuation systems" Microelectronics Reliability 39, pp1229-1237, 1999

[20] Sriram Sundararajan; Bharat Bhushan; "Static Friction and Surface Roughness Studies of Surface Micromachined Electrostatic Micromotors using an atomic force/friction force microscope"; Jour. Vac.Sci. Technol. A 19(4), Jun/Aug 2001

[21] Bharat Bhushan, Handbook of Micro/Nano Tribology, second edition, 1998

[22] H.Berney; A.Kemna; M.Hill; E.Hynes; M.O'Neill; W.Lane; "Critical Processing Issues for Micromachined sacrificial layer etching and sealing"; Sensors and Actuators; vol 76, pp356-364, 1999

[23] Meng0Ju Lin; Rongshun Chen; "Adhension Criterion for Center-anchored Circular Plates in Microstructures"; Sensors and Actuators A, vol 101, pp14-23, 2002

[24] H.Guckel; J.J.Sniegowski; T.R.Christenson; "Fabricaiton of Micromechanical Devices from Polysilicon Films with Smooth Surfaces"; Sensors and Actuators, vol 20, pp117-122, 1989

[25] Mehran Mehregany; Pradnya Nagarkar; Stephen.D.Senturia; Jeffrey H.Lang; "Operation of Microfabricated Harmonic and Ordinary Side-Drive Motors", Proceedings IEEE Micro Electro Mechanical Systems, pp344-352, February 1990

[26] Dhuler,V.R; Mehregany,M; Phillips.S.M; "Micromotor Operation in a liquid environment"; Solid-State Sensor and Actuator Workshop, 1992. 5th Technical Digest IEEE, 22-25 June 1992

[27] H.Zarrad; J.M.Chovelon; P.Clechet; N.Jaffrezic-Renault; C.Martelet; M.Belin; H. Perez; Y. Chevalier; "Optimization of Lubricants for Silica Micromotors"; Sensors and Actuators A, vol 46-47, pp598-600, 1995

[28] Zheming Zhao; Bharat Bhushan; "Effect of bonded lubricant films on the tribological performance of magnetic thin-film rigid disks"; Wear, vol 202, pp50-59, 1996

[29] J.L.Streator; B.Bhushan and D.B.Bogy; "Lubricant performance in magnetic thin film disks with carbon overcoat, part I: Dynamic and Static Friction", ASME J.Tribol., vol 113, pp22-31, 1991

[30] C.Gao; B.Bhushan; "Tribological performance of magnetic thin-film glass disks: Its relation to surface roughness and lubricant structure and its thickness"; Wear, vol 190, pp60-75, 1990

[31] A.M.Scarati; G.Caporiccio; "Friction behaviour and wear resistance of rigid disks lubricated with neutral and functional perfluoropolyethers", IEEE Trans.Magn., vol 23, 106-108, 1987

[32] James F.Doyle, Wave Propagation in Structures, An FFT-Based Spectral Analysis Mehtodology, published by Springer-Verlag New York, Inc, 1989

[33] Darle W.Dudley, "Gear Handbook, The Design, Manufacture, and Application of Gears", first edition, McGRAW-HILL BOOK COMPANY,INC, 1962

[34] David A.Koester, Ramaswamy Mahadevan, Busbee Hardy and Karen W. Markus, MUMPSs Design Handbook, Revision 7.0, Cornos Integrated Microsystems, A JDS Uniphase Company, Research Triangle Park, NC 27709.

[35] Xia Zhang and William C.Tang, "Viscous Air Damping in Laterally Driven Microresonators" Micro Electro Mechanical Systems, MEMS '94, Proceedings, pp199 – 204, 1994

[36] William C Tang; Tu-cuong H Nguyen; Michael W Judy and Roger T Howe; "Electrostatic-comb drive of lateral polysilicon resonators", Sensors and Acutators, A, vol 21-23, pp328-331, 1990

[37] Kerwin Wang, Karl F. Bohringer , Mike Sinclair and Gary Starkwether; "Highly Space-Effectient Electrostatic Zigzag Transmissive Micro-Optic Switches for an Integrated MEMS Optical Display System"; TRANSDUCERS, Solid-State Sensors, Actuators and Microsystems, 12th Innational Conference, vol 1 , pp8-12 June 2003

[38] Jon Orloff, Handbook of Charged Particle Optics, CRC Press, Boca Raton, New York, 1997

[39] William C.Tang, Martin, G.Lim and Roger T.Howe; "Electrostatic Comb Drive Levitation and Control Method", Journal of Microelectromechanical System, vol.1, No.4, December 1992.

[40] M.G.Lim; J.C.Chang; D.P.Schultz; R.T.Howe, and R.WcV.White, Proceedings of the IEEE Third MEMS Workshop, NaPa Valley, CA, pp. 82-88, 1990

[41] PolyMUMPs FAQ, Revision 1.0, MEMSCAP

[42] Jun Cao and Clark T.-C. Nguyen; "Drive Amplitude Dependence of Micromechanical Resonator Series Motional Resistance"; Digest of Technical Papers, 10th International Conference on Solid-State Sensors and Acturtors, Sendai, Japan, June 7-10, pp1826-1829, 1999

[43] Clark T.-C.Nguyen; "An Integrated CMOS Micromechanical Resonator High-Q Oscillator"; IEEE Journal of Solid-State Circuits, VOL.34, No.4, April 1999

[44] V.b.Braginsky, V.P.Mitrofanov, and V.I.Panov, Systems with Small Dissipation. Chicago, IL, Univ. Chicage Press. 1985

PUBLICATION

Yanxia Zhang, M.Kahrizi, "Stability investigation of surface micromachined comb drive at resonance", IEEE Canadian Conference on Electrical and Computer Engineering, May 1-4,2005, accepted